Materials Today Chemistry 58 (2026) 104187

Contents lists available at ScienceDirect

Materials Today Chemistry

journal homepage: www.journals.elsevier.com/materials-today-chemistry/

Engineering ionic transport in WO_3 and MoO_3 containing silver borophosphate glasses through mixed glass-former chemistry

Tomáš Hostinský [a,b,*], Petr Mošner [a], Ladislav Koudelka [a], Helena Drobná [c], Ludvík Beneš [d], Stanislav Slang [d], Adéla Jiříčková [e], Lionel Montagne [f], Andrew Rankin [g], Gregory Tricot [h], Hervé Vezin [h], Maksym Buryi [b], Sara Marijan [i], Luka Pavić [i]

[a] Department of General and Inorganic Chemistry, Faculty of Chemical Technology, University of Pardubice, 532 10, Pardubice, Czech Republic
[b] Institute of Plasma Physics of the Czech Academy of Sciences, U Slovanky 2525/1a, Prague 8, 182 00, Czech Republic
[c] Department of Physical Chemistry, Faculty of Chemical Technology, University of Pardubice, 532 10, Pardubice, Czech Republic
[d] Center of Materials and Nanotechnologies, Faculty of Chemical Technology, University of Pardubice, nam. Cs. legii 565, Pardubice, 53002, Czech Republic
[e] Department of Inorganic Chemistry, Faculty of Chemical Technology, University of Chemistry and Technology, Technická 5, 166 28 Praha 6, Czech Republic
[f] University of Lille, CNRS, Centrale Lille, University of Artois, UMR 8181-UCCS-Unité de Catalyse et Chimie du Solide, F-59000, Lille, France
[g] University of Lille, CNRS, INRAE, Centrale Lille, University of Artois, UAR 2638 – IMEC –Institut Michel-Eugène Chevreul, F-59000, Lille, France
[h] University of Lille, Laboratoire de Spectroscopie pour les Interactions, la Réactivité et l'Environnement, LASIRE UMR CNRS 8516, Building C4, F-59655, Villeneuve d'Ascq Cedex, France
[i] Ruđer Bošković Institute, Bijenička cesta 54, 10000, Zagreb, Croatia

ARTICLE INFO

Keywords:
Borophosphate glasses
Glass properties
Glass structure
Ionic conductivity

ABSTRACT

Understanding how mixed glass-former chemistry governs ionic transport is essential for the rational design of oxide glass electrolytes. Here, the structural origin of the nonlinear property enhancement associated with the mixed glass-former effect was investigated in $40Ag_2O$-$20WO_3$-$(40-x)P_2O_5$-xB_2O_3 and $40Ag_2O$-$20MoO_3$-$(40-x)P_2O_5$-xB_2O_3 glasses containing 0–30 mol% B_2O_3. Progressive substitution of P_2O_5 by B_2O_3 produced pronounced nonlinear changes in thermal properties, oxygen packing density, and ionic conductivity. Raman spectroscopy together with advanced one- and two-dimensional solid-state MAS NMR revealed that intermediate B_2O_3 contents maximize P–O–B connectivities and tetrahedral BO_4 units, leading to the formation of a highly integrated mixed borophosphate network. This structural regime coincides with the highest glass transition temperatures, suggesting that atomic-scale network mixing plays a key role in Ag^+ transport in homogeneous glasses. At higher B_2O_3 contents, increasing B–O–B connectivity promotes amorphous phase separation. Nevertheless, the phase-separated WO_3-containing glasses exhibited the highest ionic conductivity within the investigated series, suggesting that structural heterogeneity provides an additional mechanism for transport enhancement. EPR spectroscopy revealed low concentrations of reduced W^{5+}/Mo^{5+} centres, consistent with a predominantly ionic conduction mechanism. These results establish composition–structure–property relationships and provide design principles for developing high-conductivity mixed glass-former oxide electrolytes.

1. Introduction

Oxide glasses are attractive candidates for solid-state ionic conductors because their composition, network connectivity, and local structural environment can be varied continuously over broad ranges. Unlike crystalline electrolytes, glassy materials do not require preservation of a specific long-range crystal structure and can therefore accommodate substantial changes in the concentrations of network formers, modifiers, and intermediate oxides. This compositional flexibility provides an opportunity to tailor ion-transport properties through controlled modification of the glass network [1,2]. However, increasing the concentration of mobile ions alone is generally insufficient to optimize ionic conductivity, because ion mobility is also strongly influenced by the local coordination environment, connectivity of ion-conduction pathways, and structural organization of the surrounding network [1–3].

One strategy for modifying these characteristics is the simultaneous

* Corresponding author. Department of General and Inorganic Chemistry, Faculty of Chemical Technology, University of Pardubice, 532 10, Pardubice, Czech Republic.
E-mail address: tomas.hostinsky@upce.cz (T. Hostinský).

https://doi.org/10.1016/j.mtchem.2026.104187
Received 21 July 2026; Received in revised form 16 October 2026; Accepted 15 November 2026
Available online 19 November 2026
2468-5194/© 2026 The Authors. Published by Elsevier Ltd. This is an open access article under the CC BY license (http://creativecommons.org/licenses/by/4.0/).

incorporation of two glass-forming oxides. In mixed glass-former systems, substitution of one network former by another at constant modifier content can produce strongly nonlinear changes in ionic conductivity and may also be accompanied by nonlinear variations in thermal and mechanical properties. This phenomenon is commonly referred to as the mixed glass-former effect [4–6]. A positive mixed glass-former effect, manifested by conductivity values exceeding those expected from interpolation between the corresponding compositional limits, is particularly relevant to the design of glassy solid electrolytes [2,4,6]. Nevertheless, its microscopic origin remains difficult to establish because substitution of the glass formers alters several mutually dependent structural characteristics, including network-forming-unit populations, oxygen speciation, network connectivity, intermediate-range ordering, and the distribution of mobile ions and their conduction pathways [3–6].

Silver borophosphate glasses represent a suitable model system for studying these effects because Ag^+ ions exhibit substantial mobility in phosphate-rich networks, while substitution of P_2O_5 by B_2O_3 produces pronounced changes in glass connectivity. Early studies of silver borophosphate glasses showed that competition between trivalent and pentavalent glass formers can enhance cation diffusion [7,8]. Investigations of AgI-containing borophosphate glasses further indicated that their electrical properties are closely related to the formation of B–O–P linkages and to the relative populations of phosphate and borate structural units [9,10]. These results suggest that the mixed-network connectivity, rather than the nominal glass composition alone, plays a central role in controlling Ag^+ transport.

Advanced solid-state NMR studies have provided more direct insight into this connectivity. Elbers et al. [11] showed that in $50Ag_2O$–50 $[(B_2O_3)_x$–$(P_2O_5)_{1-x}]$ glasses, tetrahedral borate units are favoured at relatively low B_2O_3 contents, whereas trigonal borate species become increasingly important at higher borate concentrations. Their results also demonstrated that boron does not form simple BPO_4-like environments and that trigonal borate units preferentially participate in borate–borate rather than borate–phosphate connectivities. Such changes are expected to alter both the degree of structural mixing between the phosphate and borate subnetworks and the local environments available for Ag^+ migration. However, a direct correlation between these specific connectivity motifs and macroscopic ionic conductivity has not yet been established for transition-metal-containing silver borophosphate glasses.

The incorporation of WO_3 and MoO_3 provides an additional means of modifying phosphate-based glass networks. Both oxides form broad glass-forming regions in combination with phosphate compositions and can participate in the network through phosphate–tungstate or phosphate–molybdate linkages [12–17]. Previous studies have shown that changes in the local environments and connectivity of Mo- and W-based polyhedra can accompany phosphate depolymerisation [14,15,17]. In silver-containing phosphate glasses, molybdate incorporation has also been associated with enhanced Ag^+ conductivity and with the formation of phosphate units bonded to molybdenum [12,13]. These observations indicate that WO_3 and MoO_3 may influence ion transport not only through their own structural role, but also by modifying how phosphate and borate subnetworks reorganize during mixed glass-former substitution.

Building on our previous investigation of the Ag_2O–WO_3–P_2O_5 system [18], the present study examines glasses in the $40Ag_2O$–$20WO_3$–$(40-x)P_2O_5$–xB_2O_3 and $40Ag_2O$–$20MoO_3$–$(40-x)P_2O_5$–xB_2O_3 series. The Ag_2O and WO_3/MoO_3 contents were kept constant while P_2O_5 was progressively replaced by B_2O_3. This compositional strategy separates the influence of mixed glass-former chemistry from changes in the nominal concentration of mobile Ag^+ ions and transition-metal oxide. The selected base composition combines a high Ag_2O content with a sufficiently broad glass-forming range, enabling systematic investigation of structure and transport across both homogeneous and phase-separated glass compositions.

The objective was to identify the structural features responsible for the nonlinear property enhancement associated with the mixed glass-former effect and to derive composition–structure–property relationships relevant to the design of ion-conducting oxide glasses. Raman spectroscopy and advanced one- and two-dimensional solid-state NMR experiments were used to resolve the evolution of phosphate and borate species and the competing P–O–P, P–O–B, and B–O–B connectivities. EPR spectroscopy was employed to quantify reduced W^{5+} and Mo^{5+} centres and to evaluate the possible electronic contribution to charge transport, while impedance spectroscopy established the corresponding ionic conductivity trends. Particular attention was given to the transition from a highly mixed borophosphate network at intermediate B_2O_3 contents to chemically heterogeneous, X-ray-amorphous structures at high B_2O_3 contents. The results show that ionic transport is governed by a balance between mixed-network formation, phosphate depolymerisation, and the onset of amorphous phase separation. This provides a structural framework for the composition-driven design of silver-conducting borophosphate glasses and indicates that controlled amorphous heterogeneity may contribute to enhanced Ag^+ transport.

2. Experimental

Glasses in the $40Ag_2O$-$20WO_3$-$(40-x)P_2O_5$-xB_2O_3 and $40Ag_2O$-$20MoO_3$-$(40-x)P_2O_5$-xB_2O_3 series (x = 0-30 mol%) were prepared by melt quenching from $AgNO_3$ (99.8%, Penta), H_3BO_3 (99.5%, Lach-Ner), WO_3/MoO_3 (99.9%, Sigma-Aldrich) and H_3PO_4 (85 wt%, Penta) using 10 g batches. Mixed precursors in Pt crucibles were heated at 600 °C for 2 h to remove residual water and decompose $AgNO_3$, then melted at 1100 °C for 20 min in air. The melts were poured into preheated graphite moulds (200 °C). The glasses were annealed for 6 h at T_g − 10 °C and cooled to room temperature.

Most glass compositions were prepared in a single independent melting batch, from which specimens were subsequently obtained for the individual characterization methods. Additional independent batches were prepared for selected compositions to verify the reproducibility of the synthesis. In particular, the $40Ag_2O$–$20WO_3$–$10P_2O_5$–$30B_2O_3$ phase-separated glass was independently prepared four times. The parent $40Ag_2O$–$20WO_3$–$40P_2O_5$ glass was also independently prepared and characterized in our previous study [18], providing an additional reference for batch reproducibility. To minimize variations between preparations, identical precursor sources, calcination conditions, melting temperatures, and melting times were maintained throughout the compositional series. Repeated measurements performed on specimens from the same batch were not considered independent glass preparations.

Density was determined using a helium pycnometer (AccuPyc II 1340). Molar volume (V_M) was calculated as $V_M = \overline{M}/\rho$, where $\overline{M}$ is the average molar mass. Oxygen packing density (OPD) was calculated as $OPD = n_O/V_M$, where n_O is the number of oxygen atoms.

Thermal properties were measured using a TMA 402 F1 Hyperion dilatometer (Netzsch) at 5 °C min^{-1} under N_2 and a 300 mN load. The glass transition temperature (T_g) and dilatometric softening temperature (T_d) were determined from the dilatometric curves, while the coefficient of thermal expansion (α) was calculated in the 150–250 °C range. Raman spectra were recorded at room temperature in the 150–1400 cm^{-1} range using a DXR Raman spectrometer (Thermo Scientific) equipped with a 532 nm laser.

Phase-separated samples were analysed by SEM using a LYRA3 Tescan microscope operated at 10 kV after carbon coating. Chemical composition was verified by EDS using an AzTec X-Max20 detector (Oxford Instruments) at 5 kV. The amorphous nature was confirmed by XRD using a D8 Advance diffractometer (Bruker) with Cu Kα radiation.

^{31}P and ^{11}B MAS NMR spectra were recorded using Bruker AVANCE NEO 400 MHz (9.4 T) and 800 MHz (18.8 T) spectrometers, respectively. The ^{31}P and ^{11}B chemical shifts were referenced to 85% H_3PO_4 and solid

$NaBH_4$, respectively. Spectral deconvolution was performed using the DMFit software [19]. In addition to 1D MAS NMR, $^{11}B(^{31}P)$ D-HMQC, ^{11}B DQ-SQ and ^{31}P refocused INADEQUATE [20] experiments were performed to probe borophosphate connectivity. Detailed experimental parameters for all NMR measurements are provided in the Supplementary Information.

Continuous-wave EPR measurements were performed at room temperature using an X-band spectrometer (ELEXSYS E500, Bruker) operating at a microwave frequency of 9.87 GHz. The spectra were recorded under non-saturating conditions using a microwave power of 5.024 mW, a modulation amplitude of 5 G. Spectral simulations and angular fitting were performed using the Easyspin 6.0.12 toolbox program [21].

For electrical measurements, gold electrodes (6 mm diameter) were sputtered onto both sides of ~1 mm thick disks. Impedance spectra were measured using a Novocontrol Alpha-AN dielectric spectrometer in the frequency range 0.01 Hz-1 MHz between −60 and 210 °C with step of 30 °C. The impedance spectra were analysed by equivalent circuit modelling using the WinFIT software (Novocontrol Technologies). The circuit consisted of a parallel resistor–constant phase element (R–CPE) combination, representing the bulk response of the glass, connected in series with a CPE (more details in Supplementary Information) representing electrode polarization due to Ag^+ accumulation at the blocking gold electrodes. The direct current (DC) electrical conductivity, σ_{DC}, was calculated from the fitted bulk resistance as $\sigma_{DC} = t/(R \times A)$, where t is the sample thickness and A is the electrode area, and agreed with the values obtained from the low-frequency plateau of the conductivity spectra.

3. Results and discussion

3.1. General glass properties

Seven samples within the compositional series $40Ag_2O$-$20WO_3$-$(40-x)P_2O_5$-xB_2O_3 and seven samples within the series $40Ag_2O$-$20MoO_3$-$(40-x)P_2O_5$-xB_2O_3 were prepared using the standard melt-quenching technique. Pictures of prepared samples are shown in Fig. 1a. In both series, glassy samples were obtained within the compositional range of 0-25 mol% B_2O_3. The glasses containing WO_3 were characterised by a yellow colour and good transparency. In contrast, the glasses containing MoO_3 exhibited colours ranging from brown to orange. In both cases, the observed colours arise from the presence of tungsten and molybdenum in their reduced oxidation states (W^{5+} and Mo^{5+}, respectively), whose presence was confirmed using EPR. For both series, the samples containing 30 mol% B_2O_3 became opaque and lost transparency. SEM observations revealed the presence of a distinct droplet-like microstructure characteristic of phase-separated glasses (Fig. 1b–d). Nevertheless, XRD patterns remained fully amorphous for both samples, indicating that the separated domains

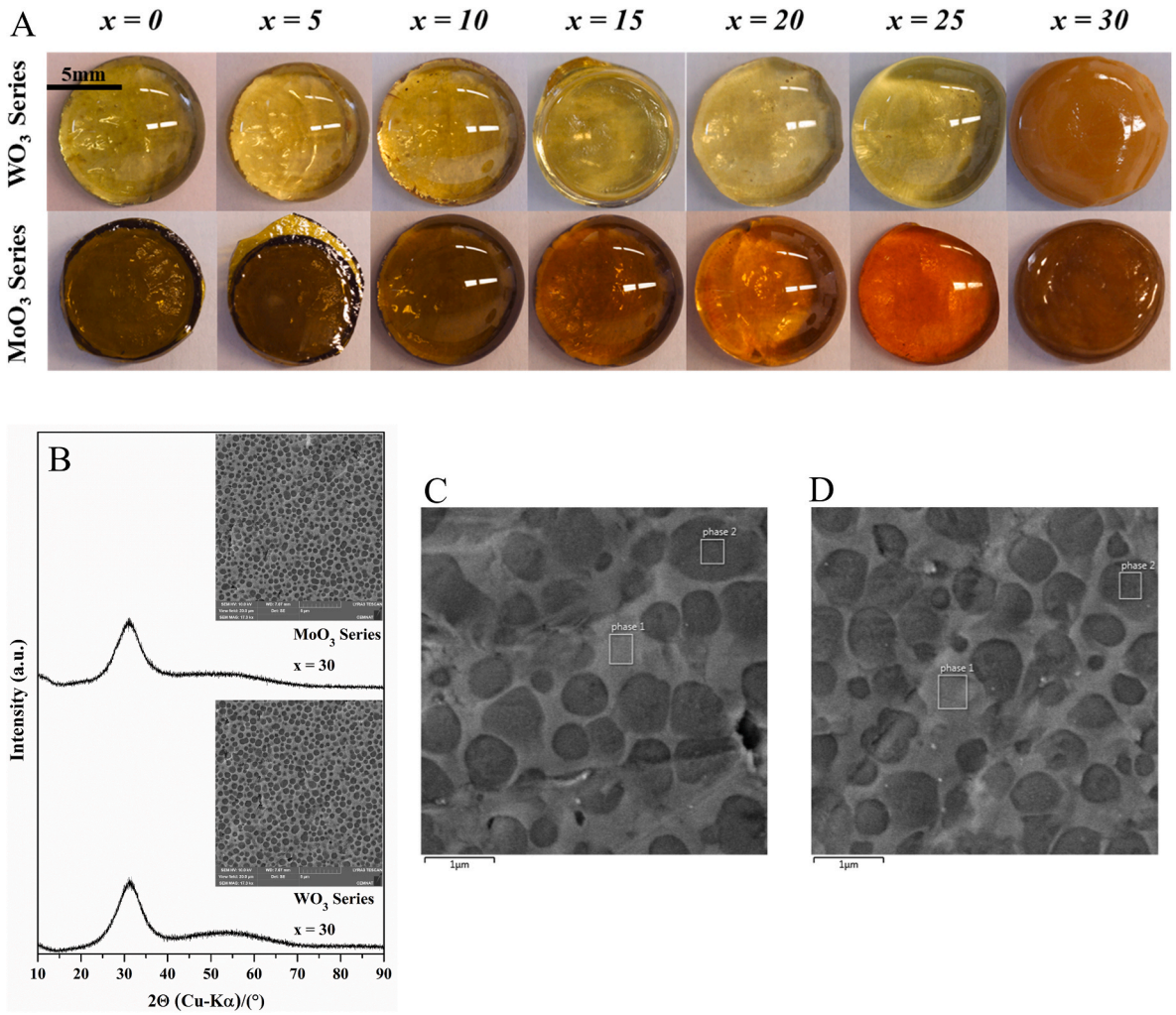

Fig. 1. (A) Photographs of glasses from the $40Ag_2O$-$20WO_3$-$(40-x)P_2O_5$-xB_2O_3 and $40Ag_2O$-$20MoO_3$-$(40-x)P_2O_5$-xB_2O_3 series. (B) XRD patterns and corresponding SEM images of phase-separated glasses with composition $40Ag_2O$-$20MO_3$-$10P_2O_5$-$30B_2O_3$ (M = W or Mo). (C, D) Regions selected for local EDX analysis in two $40Ag_2O$-$20WO_3$-$10P_2O_5$-$30B_2O_3$ samples, showing the identified Phase 1 and Phase 2 domains.

retained a glassy rather than crystalline character.

To further examine the compositional heterogeneity of the phase-separated regions, local EDX analyses were performed on the $40Ag_2O$-$20WO_3$-$10P_2O_5$-$30B_2O_3$ glass. Representative analysed regions are shown in Fig. 1c–d, while the elemental compositions are summarised in Table S1. Full-size SEM images together with the EDX spectra and elemental mapping are provided in Fig. S1–S7 (Supplementary Information). Although EDX analysis does not allow reliable quantification of boron due to its low atomic number and limited detectability in SEM-EDX measurements, measurable differences in the relative phosphorus and tungsten contents between the two regions were consistently observed, confirming the existence of chemically distinct amorphous domains.

The background phase (Phase 1) exhibited systematically higher phosphorus and tungsten concentrations, whereas the droplet-like phase (Phase 2) showed reduced phosphorus and tungsten contents together with detectable boron contributions in some analysed regions. These observations are therefore consistent with compositional partitioning accompanying amorphous phase separation in borophosphate glasses at high B_2O_3 contents. Similar behaviour has previously been reported in borophosphate systems where increasing borate concentration leads to partial incompatibility between borate-rich and phosphate-rich structural regions [22–25].

General physico-chemical properties of prepared glasses such as density, molar volume, glass transition temperature, dilatometric softening temperature, and coefficient of thermal expansion are summarised in Table 1.

The compositional dependence of glass density (ρ), molar volume (V_M), and oxygen packing density (OPD) for both glass series is shown in Fig. 2a–b. In both WO_3- and MoO_3-containing glasses, the substitution of P_2O_5 by B_2O_3 results in a progressive increase in density accompanied by a simultaneous decrease in molar volume. However, the evolution of these parameters is not linear, indicating that the observed behaviour cannot be explained solely by stoichiometric replacement effects.

A more detailed interpretation is provided by the evolution of OPD, which reflects the efficiency of oxygen atom packing within the glass network. In both glass series, OPD initially increases with increasing B_2O_3 content and reaches a maximum at approximately 10-15 mol% B_2O_3. This behaviour correlates well with the rapid increase in density observed at low B_2O_3 concentrations. In the $40Ag_2O$-$20WO_3$-(40–x) P_2O_5-xB_2O_3 series, OPD increases from 0.076 to 0.080 mol O•cm^{-3} between x = 0 and 10 mol% B_2O_3, indicating a significant improvement in structural packing efficiency. Consequently, the density rises steeply from 4.94 to 5.36 g•cm^{-3} within this compositional range. A similar but less pronounced trend is observed for the MoO_3-containing glasses, where both OPD and density increase more gradually.

The initial increase in OPD is most likely associated with the preferential formation of tetrahedral BO_4 structural units at lower B_2O_3 concentrations. In modifier-rich borophosphate glasses, BO_4 units are generally favoured due to charge compensation by Ag^+ ions and are structurally more compatible with the phosphate network [11,25,26]. Their incorporation promotes a more compact and efficiently packed glass structure, thereby enhancing density.

With further B_2O_3 addition, however, the increase in OPD slows down and eventually stagnates or slightly decreases. This behaviour suggests a gradual structural transition from BO_4 to trigonal BO_3 units, which will be investigated with ^{11}B NMR in the following. Unlike tetrahedral BO_4 groups, planar BO_3 units exhibit a greater tendency toward B–O–B linkages and partial borate clustering, reducing their compatibility with the surrounding phosphate–transition metal network. As a result, the efficiency of oxygen packing no longer improves despite the continuing decrease in molar volume. This explains why the density increase becomes significantly less pronounced above ~10-15 mol% B_2O_3 in both glass series.

The different behaviour between WO_3- and MoO_3-containing glasses may further indicate that the tungsten-containing network accommodates the initial boron incorporation more efficiently, possibly due to differences in the connectivity and rigidity of WO_6 and MoO_6 containing structural environments. This leads to a steeper OPD increase and stronger densification effect at low B_2O_3 contents, whereas the structural reorganization in the MoO_3-containing glasses proceeds more gradually.

3.2. Thermal behaviour

The data obtained from the dilatometric curves are presented in Fig. 2c–d, as well as in Table 1. A significant increase in the glass transition temperature (T_g) was observed in both glass series within the range of 0-10 mol% B_2O_3, however, further additions of B_2O_3 resulted in a decrease in T_g in the MoO_3-containing glass series and a more gradual decrease in the WO_3-containing glass series. In the $40Ag_2O$-$20WO_3$-$(40-x)P_2O_5$-xB_2O_3 glass series, both the glass transition temperature (T_g) and the dilatometric softening temperature (T_d) were found to be higher than those in the $40Ag_2O$-$20MoO_3$-$(40-x)P_2O_5$-xB_2O_3 series (see Table 1). This difference can be primarily attributed to the higher bond energy of W−O (672.0 ± 41.8 kJ/mol [27]) compared to that of Mo−O (560.2 ± 20.9 kJ/mol [27]). The increase in T_g within the 0-10 mol% B_2O_3 range correlates well with the simultaneous increase in oxygen packing density (OPD), indicating that the initial incorporation of borate units promotes a more compact and efficiently connected glass network. The compositional region corresponding to the maximum OPD (~10-15 mol% B_2O_3) also coincides with the maximum T_g observed in both glass series, suggesting that optimization of oxygen packing and network connectivity plays a key role in enhancing structural rigidity. At

Table 1
Composition and selected physical properties of $40Ag_2O-20WO_3-(40-x)P_2O_5-xB_2O_3$ and $40Ag_2O-20MoO_3-(40-x)P_2O_5-xB_2O_3$ glass series.

Batch composition (mol%)				ρ±0.02	V_M±0.5	OPD±0.001	T_g±2	T_d±1	$\alpha_{(150\text{-}250\ °C)}$ ±0.5	M^{5+}/M_{tot} ±5%
Ag_2O	WO_3	P_2O_5	B_2O_3	g•cm^{-3}	cm^3•mol^{-1}	mol O• cm^{-3}	°C		ppm/°C	%
40%	20%	40%	0%	4.94	39.6	0.076	285	305	21.1	4.13
40%	20%	35%	5%	5.15	37.4	0.078	320	348	19.7	0.62
40%	20%	30%	10%	5.36	35.2	0.080	382	405	18.6	0.42
40%	20%	25%	15%	5.40	34.2	0.079	382	406	17.9	0.20
40%	20%	20%	20%	5.46	33.2	0.078	380	402	17.8	0.14
40%	20%	15%	25%	5.51	32.3	0.078	369	392	18.2	0.05
40%	20%	10%	30%	5.62	31.0	0.078	315	335	19.0	0.04
Ag_2O	MoO_3	P_2O_5	B_2O_3							
40%	20%	40%	0%	4.45	40.0	0.075	269	283	19.8	7.59
40%	20%	35%	5%	4.65	37.6	0.077	318	335	19.2	5.17
40%	20%	30%	10%	4.78	35.8	0.078	354	375	19.2	3.02
40%	20%	25%	15%	4.88	34.3	0.079	341	355	19.6	0.50
40%	20%	20%	20%	4.91	33.3	0.078	327	347	19.9	0.35
40%	20%	15%	25%	4.97	32.2	0.078	301	321	20.3	0.04
40%	20%	10%	30%	4.97	31.5	0.076	240	263	-	0.01

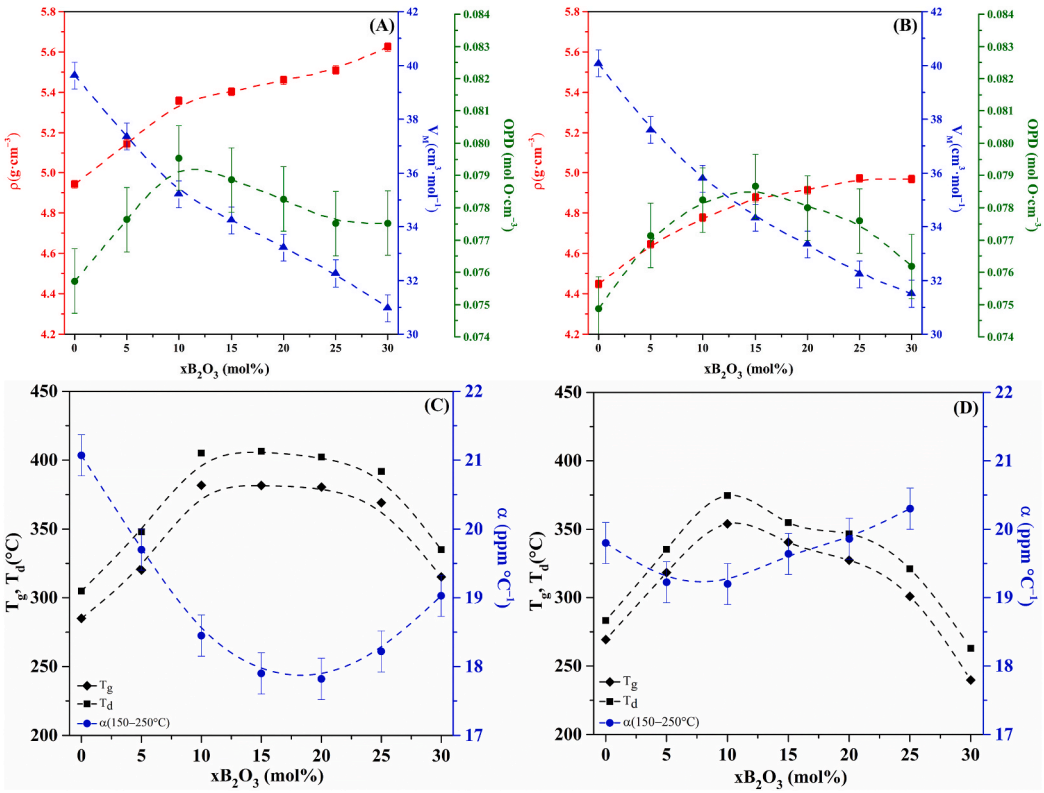

Fig. 2. Density, molar volume, and oxygen packing density of the $40Ag_2O$-$20MO_3$-$(40-x)P_2O_5$-xB_2O_3 glasses for M = W (A) and Mo (B), and TMA-derived thermal parameters of the WO_3 (C) and MoO_3 containing (D) glasses. Thermal parameters include T_g, T_d, and α. Dashed lines serve as guides to the eye. Error bars for density, T_g and T_d are smaller than the symbol size.

higher B_2O_3 contents, the gradual transformation of tetrahedral BO_4 units into trigonal BO_3 species reduces packing efficiency and promotes borate-rich structural domains, leading to a progressive decrease in T_g.

Changes in the coefficient of thermal expansion (CTE) with composition were more pronounced in the WO_3-containing glasses than in the MoO_3-containing glasses. In the WO_3-containing glass series, the CTE

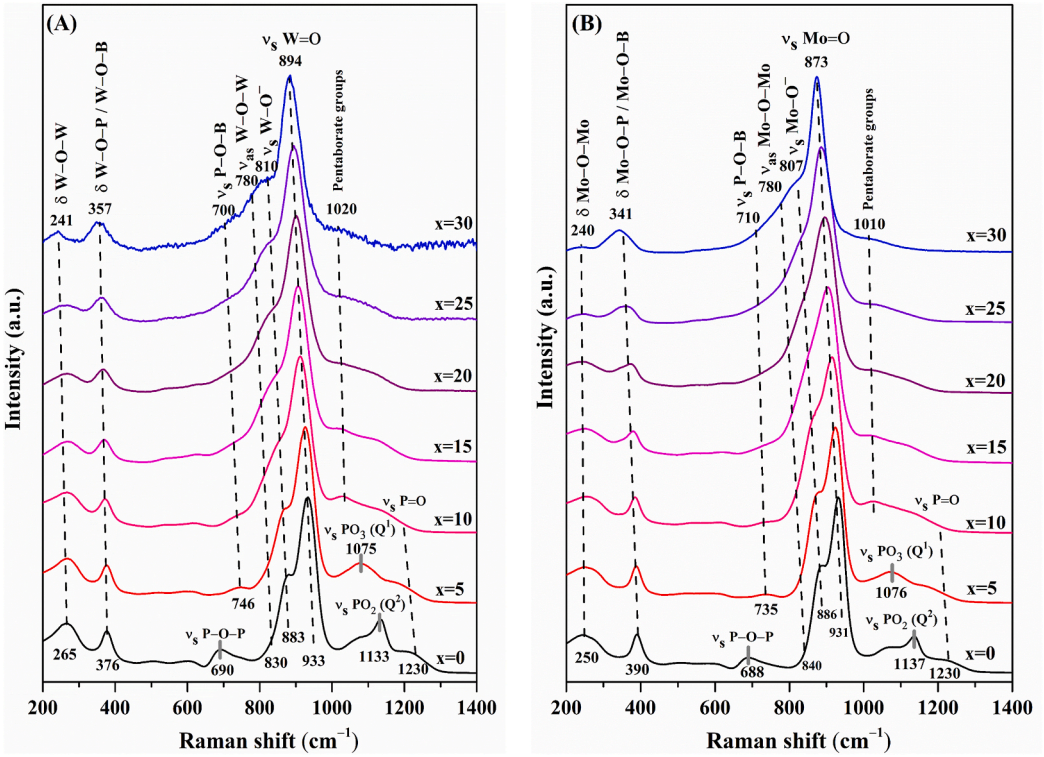

Fig. 3. Raman spectra of the $40Ag_2O$-$20WO_3$-$(40-x)P_2O_5$-xB_2O_3 (A) and $40Ag_2O$-$20MoO_3$-$(40-x)P_2O_5$-xB_2O_3 (B) glass series.

decreased from 21.1 ppm/°C at 0% B_2O_3 to a local minimum of 17.8 ppm/°C at 20% B_2O_3, after which it increased slightly to 19.0 ppm/°C at 30% B_2O_3. In contrast, the MoO_3-containing glass series exhibited a smaller overall change: the CTE decreased from 19.8 ppm/°C at 0% B_2O_3 to 19.2 ppm/°C at 5% and 10% B_2O_3, followed by a gradual increase to 20.3 ppm/°C at 30% B_2O_3. These trends reflect the influence of both compositional changes and network connectivity on the thermal expansion behaviour of the glasses, with the WO_3-containing series showing a more pronounced compositional dependence.

3.3. Structural analysis by Raman spectroscopy

Fig. 3a and b shows the Raman spectra of both glass series. The spectra exhibit generally similar features, with only minor differences in the positions of individual vibrational bands. Because of the higher Raman scattering efficiency of tungstate and molybdate structural units relative to phosphate groups, the phosphate-related bands are comparatively weak and are primarily observed in glasses containing 0–10 mol % B_2O_3. Bands located at approximately 1133 cm^{-1} in the WO_3-containing glasses and 1137 cm^{-1} in the MoO_3-containing glasses are commonly associated with symmetric stretching vibrations of PO_2^- groups in metaphosphate (Q^2) units [28–31]. Their gradual decrease in intensity and shift toward lower wavenumbers with increasing B_2O_3 content are consistent with progressive changes in phosphate speciation and network depolymerisation [28]. However, the decreasing phosphate concentration and possible overlap with other vibrational contributions may also influence the observed band intensities. Additional phosphate-related features are observed near 690 cm^{-1} (WO_3 series) and 688 cm^{-1} (MoO_3 series), which are generally attributed to symmetric stretching vibrations of bridging P–O–P bonds [28–31]. The progressive weakening of these bands is consistent with the disruption of phosphate chains, as independently supported by the ^{31}P MAS NMR results discussed below.

The formation of a mixed borophosphate network may also contribute to the evolution of several Raman features. A weak band emerging near 1100 cm^{-1} may contain contributions from borate-related vibrations, including those previously associated with pentaborate structural units [30,32], although its specific assignment remains uncertain due to spectral overlap. Furthermore, a broad feature gradually develops near 700 cm^{-1} with increasing B_2O_3 concentration. Vibrations involving P–O–B linkages may contribute to this region [30, 32], but their contribution cannot be unambiguously separated from overlapping P–O–P and other network vibrations. Nevertheless, the observed spectral evolution is consistent with the increasing incorporation of borate species into the phosphate network, as independently demonstrated by the 2D NMR experiments. Weak bands at approximately 376 cm^{-1} in the WO_3-containing glasses and 390 cm^{-1} in the MoO_3-containing glasses may include contributions from bending vibrations involving P–O–W and P–O–Mo linkages, respectively [2, 33–36], while bands near 265 cm^{-1} and 250 cm^{-1} are consistent with metal–oxygen bending vibrations involving W–O and Mo–O structural units [35–38]. The gradual broadening and intensity evolution of these low-frequency features suggest changes in the local bonding environments and connectivity of the tungstate/molybdate units during borate incorporation, although individual vibrational contributions cannot be uniquely resolved.

In the WO_3-containing glasses, the dominant high-frequency Raman band, commonly associated with terminal W═O stretching vibrations, shifts from 933 cm^{-1} at x = 0 to 894 cm^{-1} at x = 30 mol% B_2O_3. A similar but more pronounced shift is observed for the MoO_3-containing glasses, where the corresponding band, commonly associated with Mo═O stretching vibrations, shifts from 931 to 873 cm^{-1}. Previous studies have associated comparable downshifts with changes in the local coordination environments of tungsten and molybdenum, including possible transitions between distorted octahedral and tetrahedral configurations in depolymerised phosphate glasses [17,36,37]. However, the assignment of these bands in complex borophosphate systems is not unique, as their positions are also sensitive to local bond strengths, bond lengths, network connectivity, and modifier–oxygen interactions. Consequently, the observed shifts cannot be regarded as direct evidence of changes in W/Mo coordination numbers.

In the investigated glasses, progressive substitution of P_2O_5 by B_2O_3 is accompanied by substantial changes in phosphate speciation and borophosphate connectivity, as established by MAS NMR spectroscopy. These structural changes are expected to modify the distribution of oxygen environments and the local bonding arrangements surrounding tungstate and molybdate species. Previous investigations of the Ag_2O–WO_3–P_2O_5 system demonstrated that the position of the W═O Raman band is sensitive to Ag_2O concentration and overall glass connectivity [18], suggesting that Ag^+–oxygen interactions may also influence the observed spectral evolution. Accordingly, the Raman band shifts observed in the present glasses are interpreted as reflecting changes in the local W–O and Mo–O bonding environments associated with phosphate network depolymerisation and structural reorganization. Possible partial changes in W/Mo coordination environments cannot be excluded, but cannot be established unambiguously from the present Raman data.

Additional insight into the different structural behaviour of tungsten and molybdenum is provided by the targeted crystallization experiments discussed in the Supplementary Information (Fig. S8–S16). Crystallization of the WO_3-containing glasses predominantly yielded phases with octahedrally coordinated tungsten, whereas the MoO_3-containing glasses showed a greater tendency to form phases containing tetrahedrally coordinated molybdenum at high B_2O_3 contents. Although the coordination environments in the resulting crystalline phases do not necessarily reflect those present in the parent glasses, these observations reveal distinct crystallization behaviour of tungsten and molybdenum as a function of glass composition. Such differences may be consistent with the greater sensitivity of the local Mo–O environments to changes in the glass network, as suggested by the larger Raman band shifts observed for the Mo-containing glasses. However, the crystallization results cannot independently establish coordination changes in the amorphous state, and the Raman shifts may also reflect changes in bond lengths, bond strengths, and network connectivity. In addition to the main high-frequency W–O/Mo–O bands, shoulders located near 883 cm^{-1} in the WO_3-containing glasses and 886 cm^{-1} in the MoO_3-containing glasses may be associated with stretching vibrations of W–O and Mo–O bonds within the corresponding polyhedra. At B_2O_3 concentrations exceeding x = 15 mol%, a weak feature emerges near 800 cm^{-1} and gradually increases in intensity. Similar features have previously been associated with vibrations involving W–O–W and Mo–O–Mo linkages in transition-metal oxide networks [17,36,39]. However, contributions from other metal–oxygen vibrations cannot be excluded, and the present spectra do not allow the formation or extent of specific W/Mo polyhedral clusters to be determined unambiguously. The evolution of these bands is therefore interpreted as further evidence of changes in the local tungstate/molybdate environments rather than direct confirmation of increasing connectivity between specific polyhedral units.

Overall, Raman spectroscopy reveals substantial changes in the vibrational characteristics of the investigated glasses upon progressive substitution of P_2O_5 by B_2O_3. The observed spectral evolution is consistent with phosphate network depolymerisation, the development of mixed borophosphate connectivity, and changes in the local bonding environments of tungsten and molybdenum. However, due to the extensive overlap of vibrational bands and their sensitivity to multiple structural factors, Raman spectroscopy alone does not allow unambiguous identification of individual borate and phosphate structural species or quantitative determination of W/Mo coordination environments. Therefore, complementary structural information was obtained using multinuclear MAS NMR spectroscopy, which provides independent evidence for phosphate depolymerisation and the evolution of borophosphate connectivity.

3.4. Structural analysis by ^{31}P and ^{11}B 1D/2D NMR spectroscopy

3.4.1. 1D MAS NMR characterization

The ^{11}B and ^{31}P MAS NMR spectra of the WO_3- and MoO_3-containing glasses exhibit closely comparable compositional evolution (Fig. 4a and b). As shown by the direct overlay of the normalized spectra, analogous compositions from the two series display similar spectral line shapes and the principal resonances occur at comparable chemical shifts. In the ^{11}B MAS NMR spectra, both series show the same progressive evolution of the trigonal and tetrahedral borate environments with increasing B_2O_3 content, while the ^{31}P MAS NMR spectra reveal a comparable redistribution of phosphate environments associated with progressive phosphate-network depolymerisation. These similarities are consistent with the Raman results and indicate that substitution of P_2O_5 by B_2O_3 induces analogous structural reorganization in the WO_3- and MoO_3-containing networks.

Additional support is provided by the 2D NMR measurements of the x = 15 compositions, for which both DQ–SQ and D-HMQC spectra were acquired for the WO_3- and MoO_3-containing glasses (Fig. S17). The corresponding 2D spectra exhibit closely comparable correlation patterns, providing further evidence that the principal B–O–B and B–O–P/P–O–P connectivity motifs identified in the WO_3 series are also present in the MoO_3 analogue. This comparison does not imply identical quantitative distributions of individual structural species in the two series; rather, it supports a common qualitative structural framework and analogous compositional evolution. On this basis, the WO_3-containing series was selected for the detailed 2D NMR analysis discussed below, while the MoO_3 series is treated as a structurally analogous, but not quantitatively identical, system.

At 18.8 T, the ^{11}B MAS NMR spectra (Fig. 5a) clearly resolve the $^{[3]}B$ and $^{[4]}B$ regions. Multiple $^{[4]}B$ components are evident, whereas the $^{[3]}B$ resonance consists of a single broad signal that increases with B_2O_3 content. The ^{31}P MAS NMR spectra broaden and shift towards higher chemical shift with increasing B_2O_3 content, reflecting progressive phosphate depolymerisation ($Q^2 \rightarrow Q^1 \rightarrow Q^0$), consistent with the characteristic chemical shift regions of these phosphate species [28,40]. To obtain more detailed structural information, the spectra were decomposed using the DMFit software [19].

Prior to decomposition, the ^{11}B MAS NMR spectra were corrected for satellite transition contributions. The $^{[4]}B$ region was fitted using Gaussian functions, while the $^{[3]}B$ region was modelled using a QMAS½ function [19]. All fitted parameters are summarised in Table S2 (Supplementary Information). The evolution of borate species is presented in Fig. 5c–d as relative percentages and absolute concentrations per formula unit, respectively. The absolute concentration of structural units was calculated according to Eq. (1):

$$N_{unit} = \frac{n_{element} \cdot X_{oxide} \cdot P_{unit}}{100}$$

where $n_{element}$ represents the number of relevant atoms per oxide formula unit (e.g., 2 for B in B_2O_3), X_{oxide} is the molar fraction of the oxide, and P_{unit} is the relative fraction of the structural species.

Because the B_2O_3 content changes across the compositional series, discussing borate speciation solely in relative percentages may be misleading. Therefore, both relative and absolute concentrations are used to describe the structural evolution of the borate network.

The decomposition revealed a complex borate network consisting of four tetrahedral $^{[4]}B$ components and one trigonal $^{[3]}B$ component. As shown in Fig. 5c–d, the structure is initially dominated by tetrahedral $^{[4]}B$ species, which are progressively replaced by trigonal $^{[3]}B$ units with increasing B_2O_3 content, a behaviour commonly observed in borophosphate glasses [22,25,41–47]. Above x = 20, $^{[3]}B$ species become dominant. This structural evolution coincides with phase separation at x = 30 (Fig. 1), where the borate-rich network dominated by $^{[3]}B$ units becomes increasingly incompatible with the phosphate sub-network [22–25].

Although $^{[3]}B$ units increase monotonically with increasing B_2O_3 content, the individual $^{[4]}B$ species exhibit more complex behaviour.

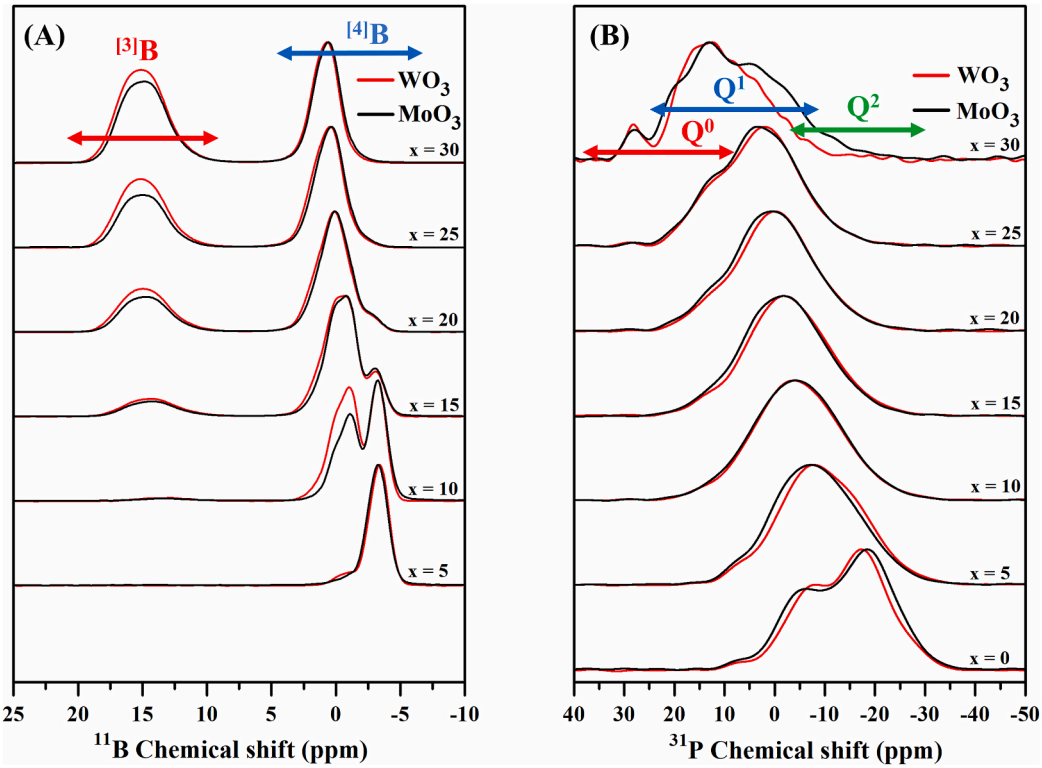

Fig. 4. ^{11}B MAS NMR (A) and ^{31}P MAS NMR (B) spectra of the $40Ag_2O$-$20MO_3$-$(40-x)P_2O_5$-xB_2O_3 glasses, where M = W (red) and Mo (black). Approximate chemical shift regions corresponding to $^{[x]}B$ and Q^n phosphate structural units are indicated.

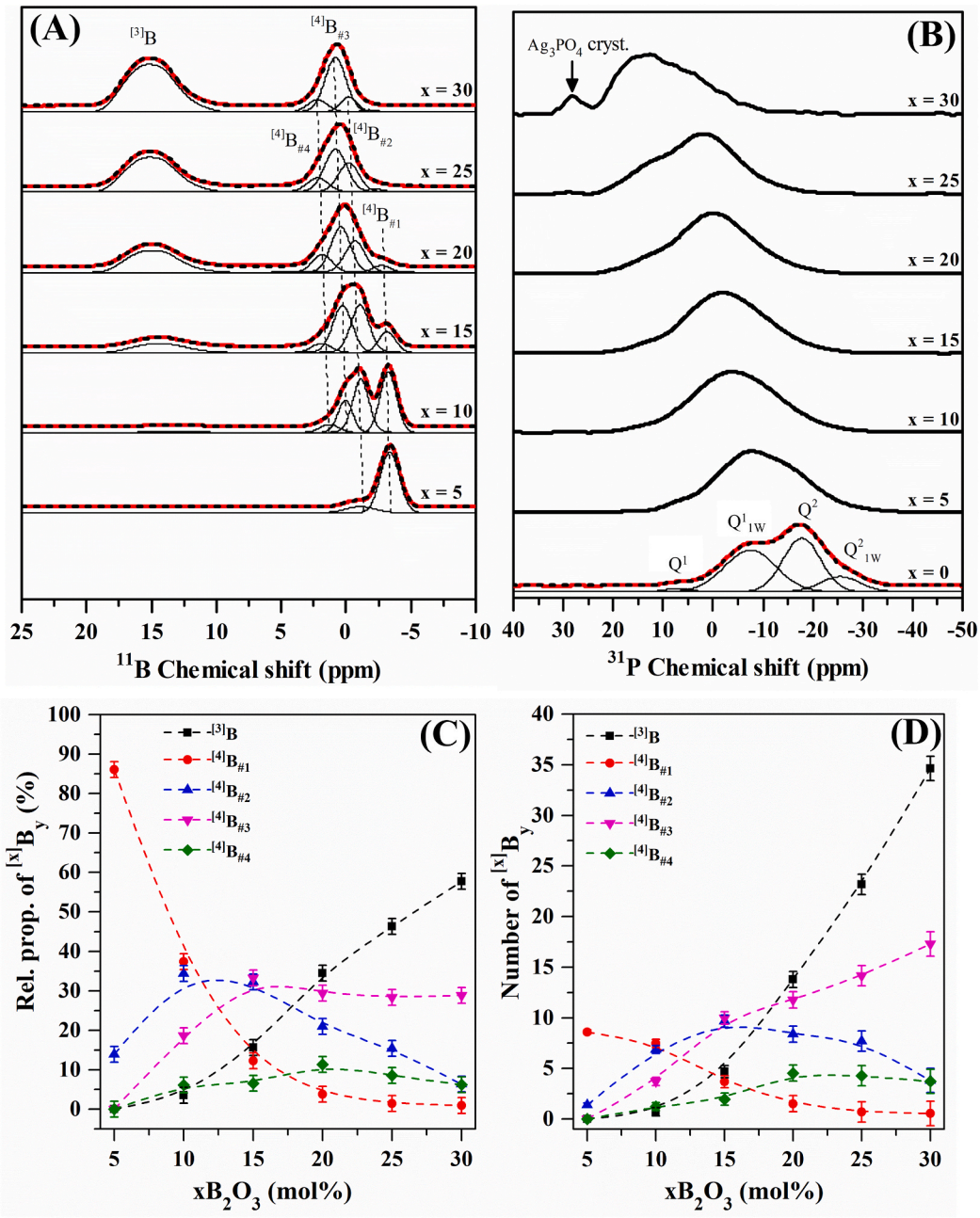

Fig. 5. ^{11}B MAS NMR (A) and ^{31}P MAS NMR (B) spectra of the $40Ag_2O$-$20WO_3$-$(40-x)P_2O_5$-xB_2O_3 glasses with corresponding spectral fits (dashed lines) and individual fitting components. Evolution of borate structural units expressed as relative fractions (C) and absolute concentrations per formula unit (D) as a function of B_2O_3 content. The estimated uncertainty of the relative populations obtained from the NMR spectral decomposition is ±2 percentage point.

Upon initial B_2O_3 addition (x = 5), two components denoted as $^{[4]}B_{\#1}$ and $^{[4]}B_{\#2}$ appear. With further boron incorporation, the intensity of $^{[4]}B\#1$ decreases, while additional $^{[4]}B_{\#3}$ and $^{[4]}B_{\#4}$ components emerge. Analysis of absolute concentrations (Fig. 5d) shows that $^{[4]}B_{\#2}$ reaches a maximum at x = 15 before slightly decreasing at higher B_2O_3 contents. In contrast, $^{[4]}B_{\#3}$ increases strongly between x = 0 and 15 and then grows more gradually, while $^{[4]}B_{\#4}$ continuously increases up to x = 20 and subsequently stabilises.

1D^{11}B MAS NMR quantifies borate species but not their connectivity. This aspect was therefore examined by correlation NMR, as will be shown in the following.

For the parent glass, decomposition of the ^{31}P MAS NMR spectrum was performed based on previous studies of related systems [2,36–39,48]. The Q^n_{mX} nomenclature is used throughout the discussion, where n denotes the number of connected phosphate units and mX the number of connected X units (X = B or W). Four phosphate components were identified: Q^2 (−17.5 ppm) and Q^1_{1W} (−6.7 ppm), which dominate the spectrum with relative populations of 48.7% and 39.5%, respectively, together with Q^2_{1W} (−26.4 ppm; 9.7%) and Q^1 (+6.5 ppm; 2.1%) species [36].

With increasing B_2O_3 content, the ^{31}P MAS NMR spectra broaden progressively due to overlap of multiple phosphate resonances with similar chemical shifts. Simultaneously, the signal maxima shift towards more positive chemical shift values, further confirming phosphate depolymerisation induced by borate incorporation. The resulting spectral complexity prevents reliable assignment of individual phosphate species based solely on one-dimensional ^{31}P MAS NMR spectra and highlights the need for advanced correlation NMR methods.

In the x = 30 glass, an additional resonance at +28.2 ppm was observed and assigned to crystalline Ag_3PO_4 based on its chemical shift and line shape [11,49], despite the absence of detectable reflections in XRD patterns. Apart from this minor sharp contribution, the overall ^{31}P MAS NMR spectrum retains the broad line shape characteristic of an amorphous material and does not exhibit sharp crystalline resonances, supporting the predominantly amorphous, yet phase separated nature indicated by XRD analysis. At the same time, the pronounced shift of the spectral maximum towards positive chemical shift values suggests a substantial increase in highly depolymerised phosphate species, particularly Q^0-type structural units.

3.4.2. *Correlation NMR - borate connectivity and borophosphate interactions*

To further investigate connectivity within the borophosphate network, 2D^{11}B DQ–SQ correlation experiments were performed to probe B–O–B linkages (Fig. 6a–d). At low B_2O_3 contents (x = 5), only weak autocorrelation of the $^{[4]}B_{\#1}$ species is observed, indicating limited borate connectivity. At higher B_2O_3 contents, additional autocorrelation signals involving $^{[4]}B_{\#2}$ and $^{[4]}B_{\#3}$ appear, indicating progressive borate network development.

At x ≥ 15, off-diagonal correlations between $^{[4]}$B and $^{[3]}$B species become visible together with a distinct $^{[3]}$B autocorrelation signal, indicating increasing participation of trigonal boron in B–O–B linkages. These features become particularly pronounced at x = 25, where $^{[3]}$B–$^{[3]}$B correlations dominate and the $^{[4]}B_{\#1}$ signal nearly disappears, suggesting a reduced structural role of this species in boron-rich glasses.

Additional information regarding P–O–B connectivity was obtained from the 2D^{11}B(^{31}P) D-HMQC spectra (Fig. 6e–h). At x = 5, two correlation signals corresponding to P–O–$^{[4]}B_{\#1}$ and P–O–$^{[4]}B_{\#2}$ linkages are observed, demonstrating that tetrahedral boron units participate directly in the mixed borophosphate framework. The position of these correlations in the ^{31}P projection (−30 to −5 ppm) further indicates that borate species interact predominantly with phosphate units belonging to the Q^2 region and effectively shortening phosphate chains.

With increasing B_2O_3 content, new correlations involving $^{[4]}B_{\#3}$ and $^{[4]}B_{\#4}$ species emerge, while the interactions remain centred primarily within the Q^2 phosphate region. In contrast, phosphate resonances observed between −5 and + 35 ppm show substantially lower intensity in the D-HMQC projections compared to the 1D^{31}P MAS NMR spectra. This behaviour indicates that phosphate species in this chemical shift region do not significantly participate in P–O–B linkages, but instead exist either as isolated Q^0 units or as phosphate species bonded preferentially to tungsten.

At x ≥ 15, weak P–O–$^{[3]}$B correlations appear, confirming partial incorporation of trigonal boron units into the mixed borophosphate network. Simultaneously, increasing differences between the $^{[3]}$B intensities in the 1D^{11}B MAS NMR spectra and the D-HMQC projections indicate that an increasing fraction of $^{[3]}$B species no longer participates in B–O–P linkages but instead forms B–O–B bonds. This observation is fully consistent with the strong $^{[3]}$B autocorrelations detected in the DQ-SQ spectra. In addition, the ^{31}P projections extracted from the D-HMQC spectra were used as a basis for decomposition of the 1D^{31}P MAS NMR spectra. The resulting decompositions, together with a detailed description of the fitting procedure, are presented in Fig. S18 (Supplementary Information).

To further clarify the structural role of individual boron species, the ^{11}B 1D MAS NMR spectra were compared with the projections extracted from the DQ-SQ and D-HMQC experiments (Fig. 7). This analysis reveals how the individual tetrahedral borate units participate in B–O–B and B–O–P connectivity as a function of composition.

At low B_2O_3 contents, $^{[4]}B_{\#1}$ and $^{[4]}B_{\#2}$ species primarily participate in B–O–P linkages, while B–O–B connectivity remains limited. Upon increasing B_2O_3 concentration, $^{[4]}B_{\#2}$ and $^{[4]}B_{\#3}$ progressively become the dominant linking units within the mixed network, simultaneously participating in B–O–P, $^{[4]}$B–O–$^{[4]}$B, and later also $^{[4]}$B–O–$^{[3]}$B connectivities. In contrast, $^{[4]}B_{\#4}$ exhibits more selective behaviour and initially participates almost exclusively in B–O–P linkages. Only at high

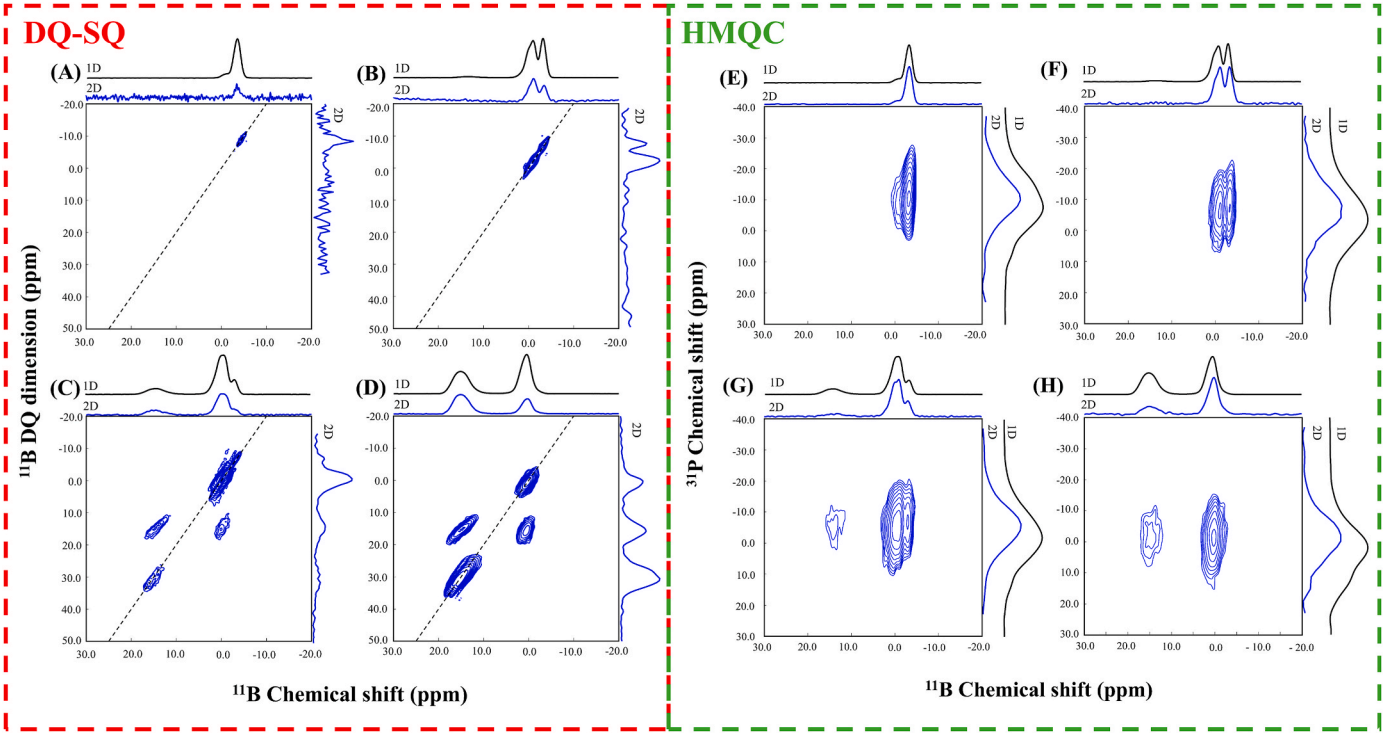

Fig. 6. 2D^{11}B DQ–SQ spectra of the x = 5 (A), 10 (B), 15 (C), and 25 (D) glasses showing B–O–B connectivities. Corresponding 1D and 2D projections are included. 2D^{11}B(^{31}P) D-HMQC spectra of the x = 5 (E), 10 (F), 15 (G), and 25 (H) glasses showing P–O–B correlations, accompanied by the ^{11}B and ^{31}P MAS NMR spectra and 2D projections.

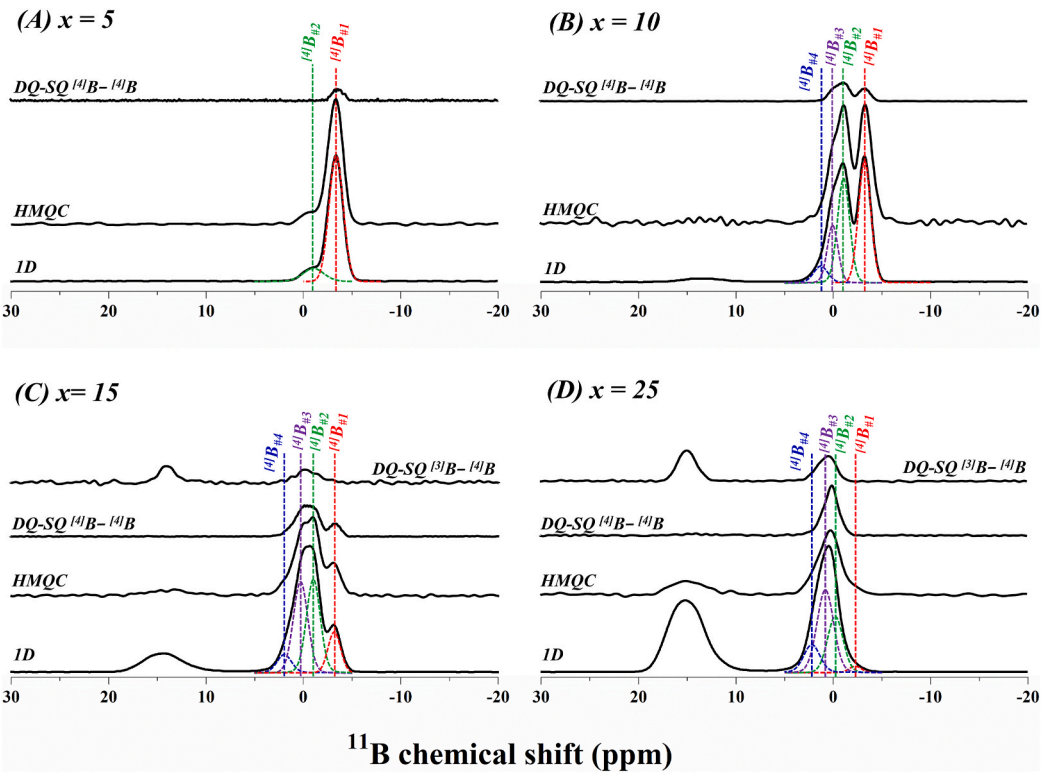

Fig. 7. Comparison of ^{11}B 1D MAS NMR spectra with projections extracted from the DQ–SQ and D-HMQC experiments for the x = 5 (A), 10 (B), 15 (C), and 25 (D) glasses. Components obtained from the 1D spectral decomposition are included to highlight differences in connectivity of individual borate species.

B_2O_3 contents does this species begin to contribute significantly to borate–borate connectivity.

A distinct reduction in the contribution of $^{[4]}B_{\#1}$ is observed with increasing B_2O_3 content. At x = 25, this species is nearly absent from the DQ-SQ spectra and remains associated primarily with B–O–P linkages. In contrast, $^{[4]}B_{\#2}$ and $^{[4]}B_{\#3}$ remain strongly involved in all observed connectivity motifs, highlighting their key role in maintaining structural integration between the phosphate and borate sub-networks.

Overall, the correlation NMR experiments demonstrate progressive separation of the borate and phosphate domains with increasing B_2O_3 content. At low boron concentrations, tetrahedral boron units efficiently integrate both sub-networks through B–O–P linkages. However, increasing formation of $^{[3]}$B species promotes preferential B–O–B connectivity, ultimately contributing to structural incompatibility between the borate-rich and phosphate-rich regions and leading to phase separation at high B_2O_3 contents.

3.4.3. Borate speciation

Borate speciation in the studied glasses was established by combining 1D and 2D^{11}B MAS NMR experiments. Four tetrahedral $^{[4]}$B species and one trigonal $^{[3]}$B species were identified (Fig. 5a), while the fitting parameters are summarised in Table S2.

The most shielded tetrahedral species, $^{[4]}B_{\#1}$ (−3.3 to −1.8 ppm), predominates at low B_2O_3 contents and participates mainly in B–O–P linkages. At compositions up to x = 15, this species forms mixed B$(OP)_3$(OB) units, as evidenced by the presence of weak $^{[4]}$B–O–$^{[4]}$B autocorrelations in the DQ–SQ spectra (Figs. 6 and 7). At higher B_2O_3 contents, however, these correlations disappear and the species becomes associated predominantly with isolated B$(OP)_4$ units. This behaviour is consistent with previous ^{11}B(^{31}P) REDOR studies performed on lithium and silver borophosphate glasses [11,44].

The $^{[4]}B_{\#2}$ species (−1.1 to −0.2 ppm) exhibits the broadest range of connectivity and participates in B–O–P, $^{[4]}$B–O–$^{[4]}$B, and $^{[4]}$B–O–$^{[3]}$B linkages, particularly at intermediate boron concentrations. Based on its intermediate chemical shift and previously reported shielding trends [22,26,44,50,51], this species is assigned to $B(OP)_{4-(n+m)}(O^{[4]}B)_n(O^{[3]}B)_m$ units, where n + m = 1–2. At higher B_2O_3 contents, its participation in linkages involving $^{[3]}$B species gradually decreases.

The $^{[4]}B_{\#3}$ species (+0.1 to +0.8 ppm) becomes dominant at x ≥ 15 and is strongly involved in the formation of extended borate subnetworks, particularly through $^{[4]}$B–O–$^{[3]}$B linkages, as demonstrated by the pronounced cross-peaks observed in Fig. 7c–d. This species is therefore assigned to $B(OP)_{4-(n+m)}(O^{[4]}B)_n(O^{[3]}B)_m$ structural units with n + m = 2-3.

The most deshielded tetrahedral component, $^{[4]}B_{\#4}$ (+1.3 to +2.2 ppm), appears primarily at high B_2O_3 contents (x ≥ 20) and exhibits only weak intensity in the correlation spectra. Its strongly deshielded chemical shift suggests a distinct local environment likely influenced by tungsten coordination. Consequently, this species is tentatively assigned to mixed units of the type $B(OP)_{4-(n+k)}(O^{[3/4]}B)_n(OW)_k$, where n = 1-2 and k = 1.

Overall, the borate speciation reveals a progressive transition from phosphorus-rich borate environments towards increasingly interconnected borate-rich and tungsten-influenced structural motifs with increasing B_2O_3 content. Simultaneously, the growing contribution of $^{[3]}$B-containing connectivities reflects gradual segregation of the borate subnetwork, ultimately contributing to phase separation at high boron concentrations [11,22,26,44–47,49–52].

3.4.4. Correlation NMR - phosphate connectivity

The P–O–P connectivities were investigated using 2D^{31}P INADEQUATE NMR spectroscopy [20], which probes direct phosphate-phosphate linkages through scalar (J) couplings (Fig. 8). Diagonal resonances correspond to Q^n–Q^n autocorrelations, while off-diagonal signals reflect connectivities between different phosphate species. To facilitate interpretation, selected slices extracted from the 2D maps are shown in Fig. 8b–d for the x = 0 and x = 5 samples,

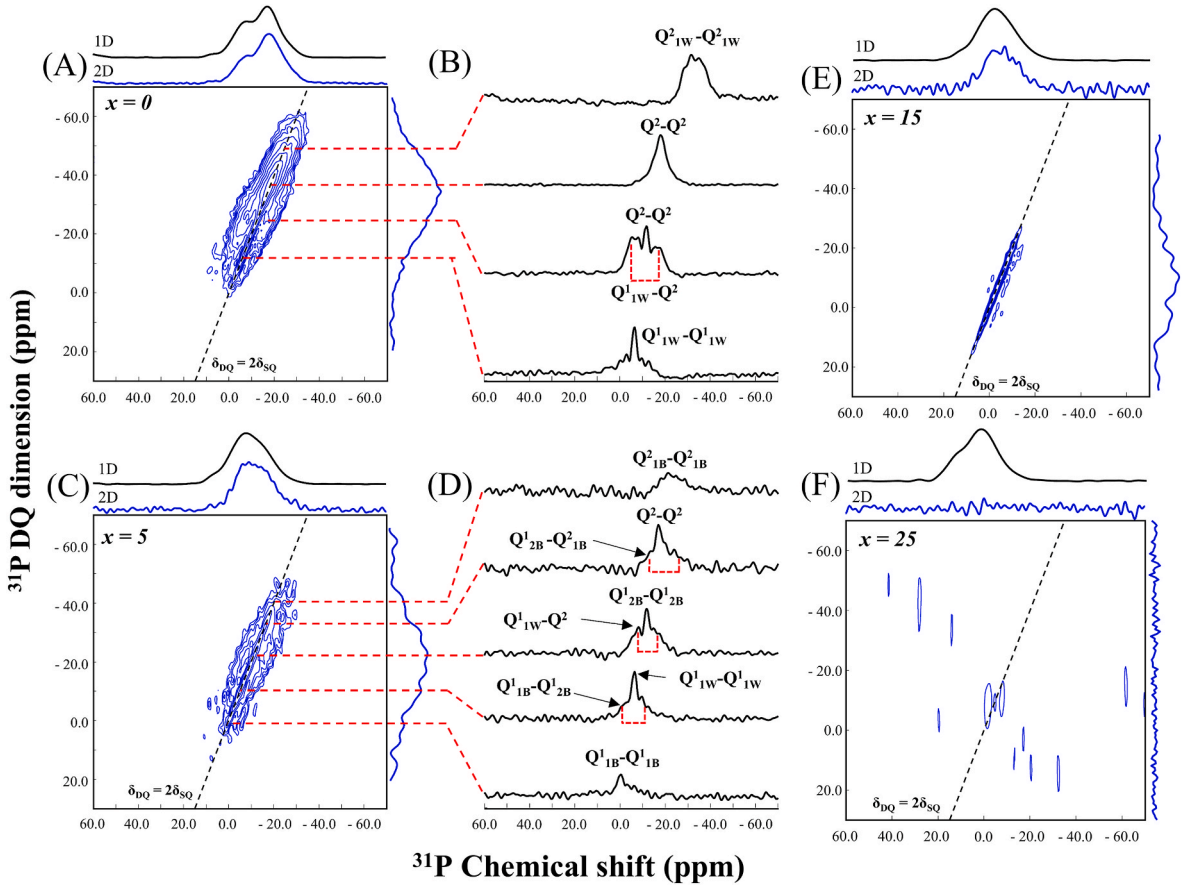

Fig. 8. 2D ^{31}P INADEQUATE NMR spectra obtained for x = 0 (A), 5 (C), 15 (E) and 25 (F) samples. The slices (B, D) show proximities between individual Q^n species for samples x = 0 and 5. The dashed diagonal line in each spectrum denotes the $\delta_{DQ} = 2\delta_{SQ}$ autocorrelation region.

respectively.

In the parent x = 0 glass (Fig. 8a–b), a relatively complex correlation pattern indicates a well-connected phosphate network. As predicted from the 1D ^{31}P MAS NMR spectra (Fig. 5b), the dominant feature is a strong Q^2–Q [2] autocorrelation signal associated with phosphate chain segments. Off-diagonal correlations between Q^1_{xW} and Q^2 species confirm that Q^1_{xW} units participate directly in the phosphate network. Additional autocorrelation signals assigned to Q^1_{xW}–Q $[1]_{xW}$ and Q^2_{1W}–Q $[2]_{1W}$ connectivities are also observed.

Interestingly, the Q^2_{1W} species does not exhibit detectable off-diagonal correlations with other phosphate units. This behaviour suggests that these species may preferentially form closed or ring-like phosphate motifs connected to the surrounding structure mainly through tungstate units rather than direct P–O–P linkages. In contrast, the remaining phosphate species display mutual off-diagonal correlations, confirming their participation in a more interconnected phosphate framework. No autocorrelation signal corresponding to the weak Q^1 species observed in the 1D ^{31}P spectra was detected in the 2D maps, likely due to their very low abundance (~2%).

With incorporation of B_2O_3, the overall intensity of the correlations decreases, reflecting progressive depolymerisation of the phosphate network. In the x = 5 sample (Fig. 8c–d), the correlation pattern becomes more complex due to the presence of borophosphate structural units. Approximate assignments of the observed signals were performed using the chemical shift positions obtained from decomposition of the ^{31}P projections extracted from the D-HMQC spectra (Fig. S18). The extracted slices show that the phosphate species remain relatively non-selectively interconnected, supporting the formation of a mixed borophosphate network. This increased structural mixing is consistent with the simultaneous increase in OPD and T_g observed at low B_2O_3 contents.

At x = 15 (Fig. 8e), only a weak Q^1 correlation remains, indicating substantial fragmentation of phosphate chains. For x = 25 (Fig. 8f), no significant autocorrelation signals are detected, suggesting that phosphate units become increasingly involved in bonding with borate and tungstate species rather than forming extended P–O–P chains.

3.4.5. *Phosphate speciation*

Phosphate speciation was established using information obtained from the 2D correlation NMR experiments. The ^{31}P projections extracted from the ^{11}B(^{31}P) D-HMQC spectra were first decomposed using the minimum number of components required to describe the borophosphate species and subsequently used as input for fitting of the 1D ^{31}P MAS NMR spectra. For the parent glass, the decomposition was based on the Q^2, Q^2_{1W}, Q^1_{1W}, and Q^1 species identified previously. Representative spectral fits are shown in Fig. 9, while all fitting parameters are summarised in Table S3. The decomposition of the x = 30 spectrum was not performed due to phase separation.

With increasing B_2O_3 content, the phosphate network undergoes pronounced structural reorganization accompanied by progressive depolymerisation. As shown in Figs. 9 and 10a–b, the initial Q^2 and Q^2_{1W} species gradually decrease, while mixed borophosphate units become increasingly dominant. Already at x = 5, new Q^2_{1B}, Q^1_{1B}, and Q^1_{2B} species appear, reflecting direct incorporation of borate units into the phosphate network. Simultaneously, the concentration of highly depolymerised Q^0-type species progressively increases. At high B_2O_3 contents, phosphate units connected exclusively to borate or tungstate species dominate, whereas phosphate–phosphate connectivities become strongly suppressed, in agreement with the ^{31}P INADEQUATE results (Fig. 8).

The evolution of the calculated X–O–Y connectivities derived from the combined ^{11}B and ^{31}P MAS NMR data is shown in Fig. 10c, while

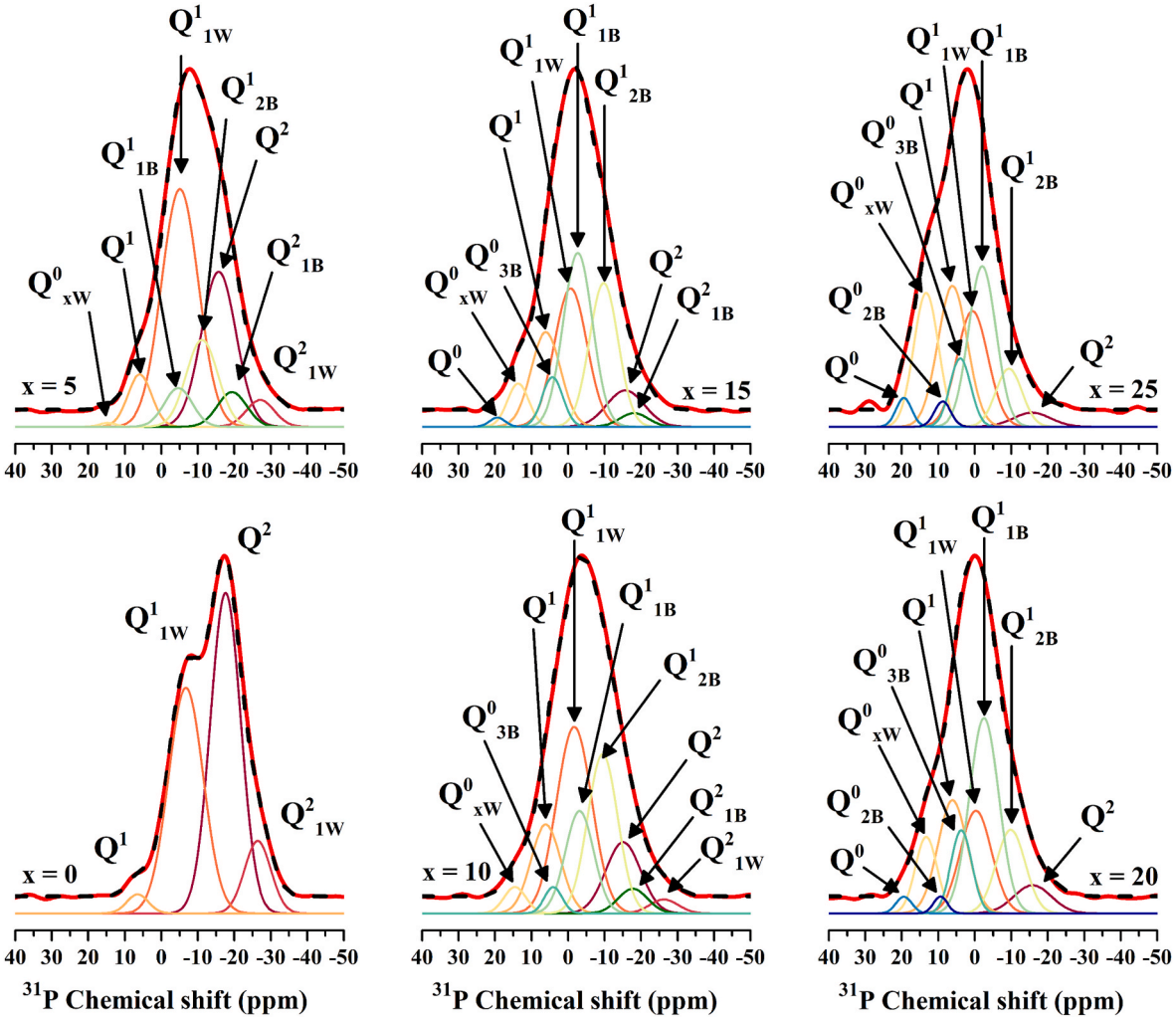

Fig. 9. 1D ^{31}P MAS NMR spectra (red line) accompanied with the fits (dashed line) and individual components used to decompose the spectra of glasses in the $40Ag_2O$-$20WO_3$-$(40-x)P_2O_5$-xB_2O_3 system.

details of the calculation procedure are provided in the Supplementary Information. The number of P–O–P linkages decreases sharply with increasing B_2O_3 content, whereas the concentration of P–O–B bonds increases up to x = 15, confirming the formation of a highly mixed borophosphate network. Above x = 15, the concentration of P–O–B bonds decreases and B–O–B connectivities become dominant. This behaviour is consistent with the increasing fraction of trigonal $^{[3]}$B units, which preferentially form borate-rich subnetworks. In contrast, the number of P–O–W bonds decreases only slightly and remains nearly constant above x = 15, indicating that tungstate units remain incorporated within the glass structure even at high B_2O_3 contents. At the same time, part of the P–O–W connectivity likely transforms into W–O–W linkages, leading to the formation of tungstate-rich structural motifs or short tungstate chains, consistent with the W–O–W vibrations observed in the Raman spectra (Fig. 3a). Similarly, the formation of B–O–W linkages associated with the $^{[4]}B_{\#4}$ species cannot be excluded, although these connectivities also cannot be quantified directly from the available experimental data.

The experimentally derived O/P values obtained from the ^{31}P MAS NMR decompositions remain nearly constant across the compositional series (Fig. 10d), whereas the theoretical O/P ratio increases continuously with increasing B_2O_3 content. Details of the O/P calculations are described in the Supplementary Information. The increasing difference between the theoretical and experimentally derived O/P values indicates that a progressively larger fraction of oxygen atoms becomes located outside the phosphate network. Approximate concentrations of oxygen atoms participating in B–O–B linkages, estimated from the combined ^{11}B MAS NMR and D-HMQC analyses, account for a substantial part of this difference and increase strongly with B_2O_3 content. The remaining oxygen atoms are therefore most likely associated with non-bridging oxygens and/or oxygen atoms involved in tungsten-containing connectivities such as W–O–W bridges.

3.5. EPR spectroscopy

EPR spectra of Mo- and W-containing glasses are shown in Fig. 11a–c. The relative fractions of reduced molybdenum and tungsten species (Mo^{5+}/Mo_{total} and W^{5+}/W_{total}) are shown in the insets and summarised in Table 1. These values were estimated from the double-integrated EPR signal intensities using a calibrated reference standard with a known spin concentration. In all compositions, the detected signals originate exclusively from Mo^{5+} and W^{5+} centres, with no additional paramagnetic species. The Mo-based glasses exhibit two contributions assigned to crystalline-like (Mo_C) and amorphous (Mo_A) Mo^{5+} environments (Fig. 11b), while three centres (W_C, W_A, and W_{AA}) were identified in the W-containing glasses (Fig. 11d). The assignments are supported by simulations based on the spin-Hamiltonian formalism [53–57]. Detailed fitting procedures, spin-Hamiltonian parameters, and discussion of individual paramagnetic centres are provided in the Supplementary Information.

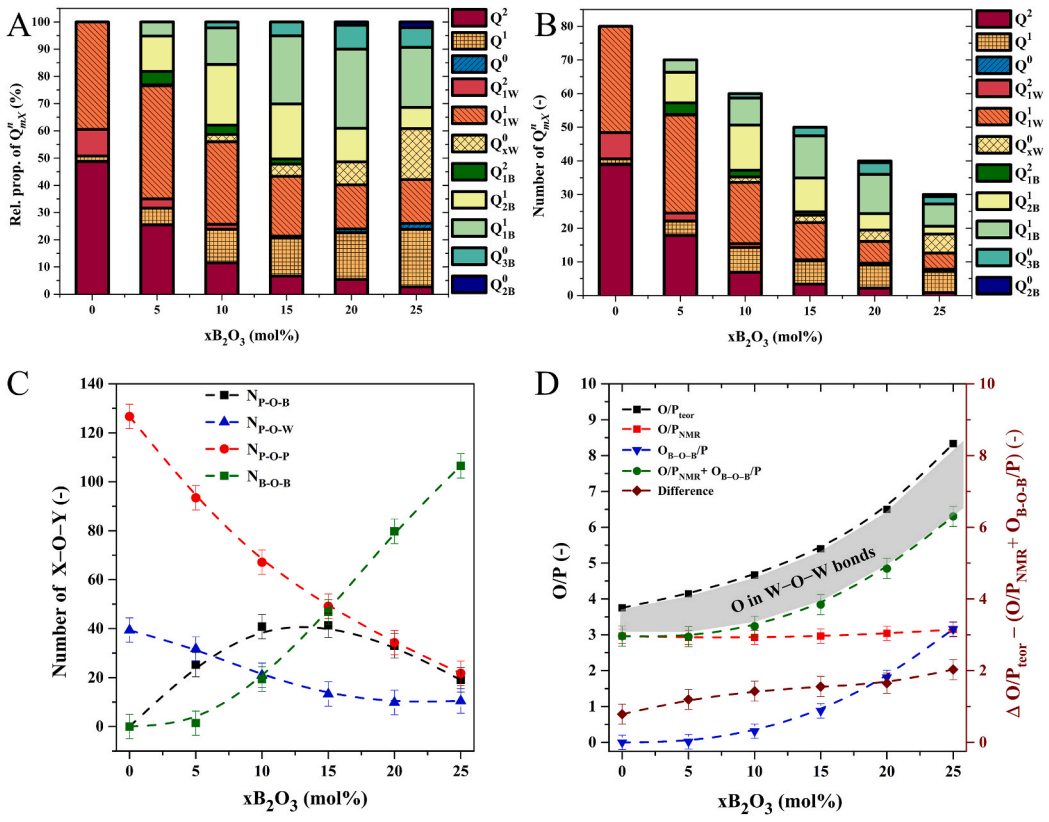

Fig. 10. Evolution of phosphate speciation expressed as relative percentages (A) and absolute numbers of structural units per formula unit (B), evolution of X–O–Y connectivities (C), and comparison of theoretical and experimentally derived O/P values (D) for the $40Ag_2O$-$20WO_3$-$(40-x)P_2O_5$-xB_2O_3 glass system. The estimated uncertainties are ±2 percentage point for the relative structural populations, ±5 for the calculated X–O–Y connectivities (C), and ±0.2 for the NMR-derived O/P ratios (D).

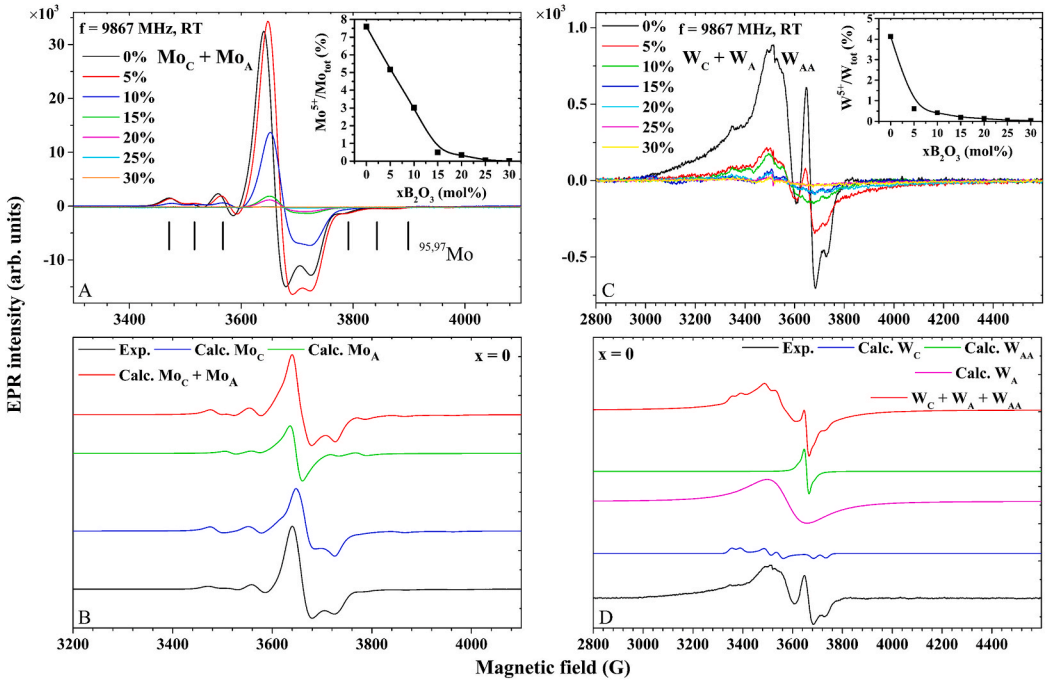

Fig. 11. The EPR spectra of glasses in the $40Ag_2O$-$20WO_3$-$(40–x)P_2O_5$-xB_2O_3 system, for both Mo- and W-based glass hosts with varying B_2O_3 content. Panels A and C present the EPR spectra together with insets showing the relative M^{5+}/M_{total} ratio (%) as a function of B_2O_3 concentration. Panels B and D show the deconvolution of the spectra measured for glasses with x = 0 into the individual Mo_C/Mo_A and W_C/W_A centres, respectively.

The anisotropic Mo_C signal is attributed to Mo^{5+} ions located in locally ordered crystalline-like environments, whereas the isotropic Mo_A

contribution originates from Mo^{5+} ions in the surrounding amorphous environment. Both centres exhibit systematic changes in g and hyperfine parameters with increasing B_2O_3 content, reflecting modifications of the local crystal field and Mo–O bonding environment [56,58–60]. Simultaneously, the EPR-quantified fraction of reduced molybdenum species (Mo^{5+}/Mo^{total}) decreases continuously with increasing B_2O_3 concentration, from 7.59% for the B_2O_3-free glass to only 0.01% at 30 mol% B_2O_3. This trend provides quantitative evidence for a pronounced decrease in the concentration of EPR-active Mo^{5+} centres. The decrease is consistent with a shift towards diamagnetic Mo^{6+} species, potentially associated with changes in the local oxygen coordination environment and redox equilibrium accompanying the increasing B_2O_3 content. However, EPR spectroscopy alone cannot unambiguously establish the oxidation state of the remaining EPR-silent molybdenum species.

The W-containing glasses exhibit significantly weaker EPR signals compared to the Mo-based compositions but display similarly complex spectral features [54,55]. Spectral simulations suggest the presence of three distinguishable W^{5+} environments corresponding to W_C, W_A, and W_{AA} centres. The W_C centre exhibits pronounced anisotropy and resolved hyperfine interactions, whereas the W_A and W_{AA} contributions are characterized by broader isotropic signals associated with more disordered local environments. The W_{AA} signal disappears entirely above 10 mol% B_2O_3, indicating progressive modification of the local tungsten environment with increasing borate content. Additional details regarding the spectral decomposition and assignment of the individual W^{5+} centres are discussed in the Supplementary Information.

Similarly to the Mo-based glasses, the EPR-quantified fraction of reduced tungsten species (W^{5+}/W^{total}) decreases strongly with increasing B_2O_3 content, from 4.13% for the B_2O_3-free glass to only 0.04% at 30 mol% B_2O_3. This pronounced decrease in the concentration of EPR-active W^{5+} centres is consistent with a progressive shift towards diamagnetic W^{6+} species as the local tungsten environment evolves with increasing borate content.

Importantly, despite the relatively high concentration of WO_3/MoO_3 in the investigated glasses, the fraction of reduced W^{5+}/Mo^{5+} centres remains very low in all compositions. This indicates that any possible contribution of electron hopping between reduced transition-metal centres to the overall transport properties is expected to be minor compared to the dominant Ag^+ based transport mechanism discussed later in the electrical conductivity section.

3.6. Electrical properties

The electrical conductivity spectra of the investigated glasses exhibit the typical behaviour of ionically conducting amorphous materials. As illustrated in Fig. 12a for the representative $40Ag_2O$-$20WO_3$-$40P_2O_5$ glass, each conductivity isotherm consists of a low-frequency DC plateau corresponding to long-range migration of Ag^+ ions and a high-frequency dispersive region associated with localized ionic motion. With increasing temperature, the onset of dispersion shifts toward higher frequencies. At temperatures above −30 °C, electrode polarization becomes visible at low frequencies due to the accumulation of mobile Ag^+ ions at the blocking gold electrodes.

The temperature dependence of the DC conductivity, σ_{DC}, for both glass series follows Arrhenius behaviour (Fig. 12b and c), indicating thermally activated ionic transport according to Eq. (3):

$$\sigma_{DC}T = \sigma_0^* e^{-E_{DC}/k_B T}$$

where σ_{DC} is the DC conductivity, σ_0* is the pre-exponential factor, k_B is the Boltzmann constant, and T is the temperature in K. The values of σ_{DC} @30 °C and E_{DC} for all investigated glasses are listed in Table 2. The σ_{DC} @30 °C and E_{DC} for the studied glasses fall within the range of approximately $10^{-6.5}$-10^{-5} Ω^{-1} cm^{-1} and 0.37-0.52 eV, respectively, aligning with the values reported for similar silver borate-phosphate glass systems [7–10].

The compositional dependences of σ_{DC} and E_{DC} are shown in Fig. 13a–b. In both glass series, gradual substitution of P_2O_5 by B_2O_3 results in a non-monotonic evolution of σ_{DC} characteristic of a nonlinear conductivity enhancement associated with the mixed glass-former effect (MGFE) [2,4–6,9,61–64]. The most pronounced increase in the electrical conductivity is observed at 10 mol% B_2O_3, where σ_{DC} is higher than that of the B_2O_3-free glass by 0.77 orders of magnitude in the WO_3 series and 0.82 orders of magnitude in the MoO_3 series. Thereafter, σ_{DC} remains nearly constant up to 25 mol% B_2O_3. A further increase to 30 mol% B_2O_3 leads to a sudden rise in conductivity, likely associated

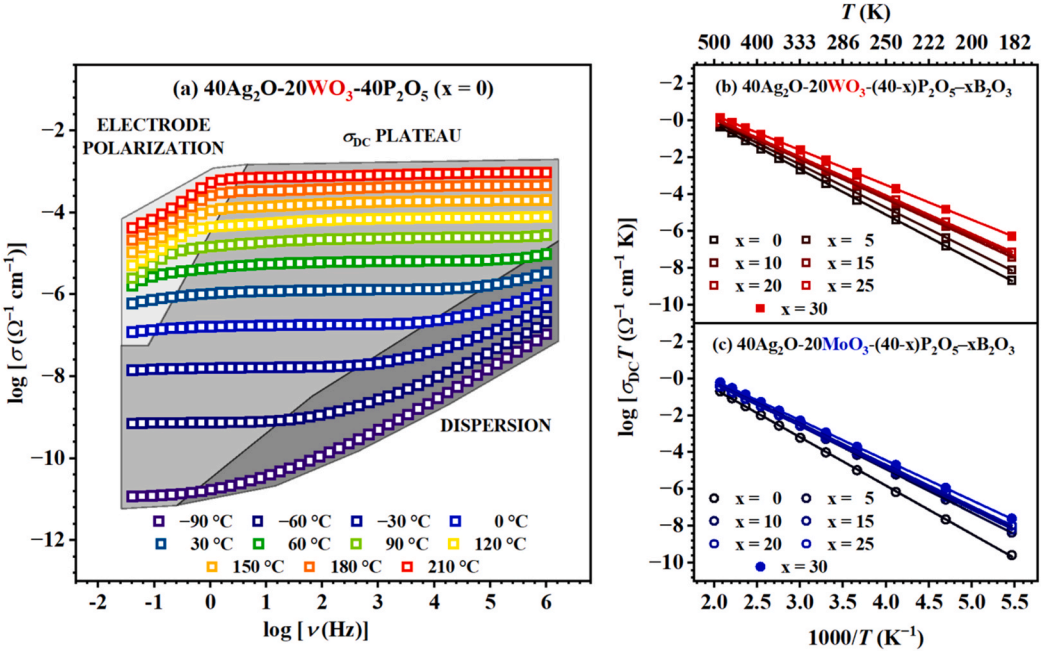

Fig. 12. (A) Conductivity spectra at different temperatures for the $40Ag_2O$-$20WO_3$-$40P_2O_5$ glass, and Arrhenius plots of DC conductivity for glasses from series (B) $40Ag_2O$-$20WO_3$-$(40-x)P_2O_5$-xB_2O_3 and (C) $40Ag_2O$-$20MoO_3$-$(40-x)P_2O_5$-xB_2O_3. The lines connecting data points in (B, C) are obtained through linear regression.

Table 2
The number density of silver ions, N_V (Ag^+), DC conductivity, σ_{DC}, @30 °C, and the activation energy for DC conductivity, E_{DC}, for glasses from series $40Ag_2O$-$20WO_3$-$(40-x)P_2O_5$-xB_2O_3 and $40Ag_2O$-$20MoO_3$-$(40-x)P_2O_5$-xB_2O_3.

	$40Ag_2O$-$20WO_3$-$(40-x)P_2O_5$-xB_2O_3			$40Ag_2O$-$20MoO_3$-$(40-x)P_2O_5$-xB_2O_3		
x	N_V (Ag^+)[a]	σ_{DC} @30 °C[b]	E_{DC}	N_V (Ag^+)[a]	σ_{DC} @30 °C[b]	E_{DC}
mol %	10^{22} cm^{-3}	Ω^{-1} cm^{-1}	eV	10^{22} cm^{-3}	Ω^{-1} cm^{-1}	eV
0	1.22	1.28×10^{-6}	0.49	1.20	3.23×10^{-7}	0.52
5	1.29	2.69×10^{-6}	0.46	1.28	1.25×10^{-6}	0.47
10	1.37	7.56×10^{-6}	0.42	1.35	2.15×10^{-6}	0.45
15	1.41	5.76×10^{-6}	0.43	1.40	2.49×10^{-6}	0.45
20	1.45	7.10×10^{-6}	0.42	1.45	1.92×10^{-6}	0.45
25	1.49	8.50×10^{-6}	0.41	1.49	1.50×10^{-6}	0.46
30	1.56	2.32×10^{-5}	0.38	1.53	3.66×10^{-6}	0.43

with the onset of phase separation in these glasses, bringing the overall enhancement relative to the B_2O_3-free glass to 1.26 orders of magnitude in the WO_3-containing series and 1.05 orders of magnitude in the MoO_3-containing series. As expected, E_{DC} exhibits an inverse trend relative to σ_{DC}, decreasing from 0.49 to 0.38 eV (WO_3 series) and from 0.52 to 0.43 eV (MoO_3 series) between 0 and 30 mol% B_2O_3. Furthermore, the WO_3-containing glasses consistently show σ_{DC} values 0.3–0.8 orders of magnitude higher at 30 °C than their MoO_3-containing counterparts, consistent with previous studies [2].

The observed conductivity trends correlate well with the structural evolution of the glass network and with the compositional dependence of T_g (Fig. 2). In particular, the most pronounced enhancement of σ_{DC}, reached at 10 mol% B_2O_3, coincides with the maximum T_g observed in both series, indicating a high degree of connectivity between phosphate, tungstate/molybdate, and borate structural units within the mixed glass network. MAS NMR analysis further reveals that gradual incorporation of B_2O_3 leads to depolymerisation of the phosphate subnetwork and disruption of phosphate ring structures present in B_2O_3-free glasses. The resulting mixed phosphate-borate network therefore appears to provide more favourable pathways for Ag^+ ion migration.

Despite the relatively high WO_3/MoO_3 content (20 mol%), several observations indicate that the electronic contribution from W^{5+}/Mo^{5+} centres is negligible and that the dominant mechanism of electrical conductivity is ionic. First, all glasses exhibit pronounced electrode polarization at low frequencies (Fig. 12a), caused by the accumulation of Ag^+ ions at the blocking gold electrodes, a direct signature of ionic transport. Second, the fraction of reduced W^{5+}/Mo^{5+} species is low (Fig. 11, Table 1) and decreases markedly with increasing B_2O_3 content while σ_{DC} increases (Fig. 13a–Table 2). Third, Summerfield scaling yields temperature-independent master curves for all glasses, indicating a single conduction mechanism over the entire temperature range (see Fig. S19a, a detailed scaling analysis is provided in the Supplementary Information).

These observations are consistent with our previous studies of WO_3/MoO_3-containing phosphate glasses. Although the fraction of reduced transition-metal ions has generally been considered relevant for polaronic conduction [65,66], polaronic transport in these glasses was shown to be governed primarily by the glass structure [67–69]. In WO_3-containing glasses, it requires connected W–O–W pathways, which form only at much higher WO_3 contents, whereas in MoO_3-containing glasses it is hindered by the cross-linking of molybdate and phosphate units, even at high Mo^{5+} fractions. Accordingly, in related Ag_2O–ZnO–P_2O_5 glasses, predominantly polaronic conduction emerged only above 40 mol% WO_3, whereas MoO_3-containing glasses remained ionic conductors up to 50 mol% MoO_3 [33,67–69]. Taken together, these results demonstrate that electrical conduction in both glass series is predominantly ionic, consistent with the purely ionic conduction observed in alkali tungstate and molybdate phosphate glasses [2,33].

4. Structure–property correlations and implications for glass design

The combined structural analysis indicates that the physical properties of the $40Ag_2O$–$20MO_3$–$(40-x)P_2O_5$–xB_2O_3 glasses are related not simply to the nominal B_2O_3 content, but to the extent and character of mixing between the phosphate and borate subnetworks. The most informative structural descriptors are the number of P–O–B linkages and the population of the $^{[4]}B_{\#2}$ units, both of which exhibit pronounced maxima at intermediate B_2O_3 contents. Their compositional evolution correlates with the nonlinear variations in T_g, oxygen packing density, and ionic conductivity summarised in Fig. 14.

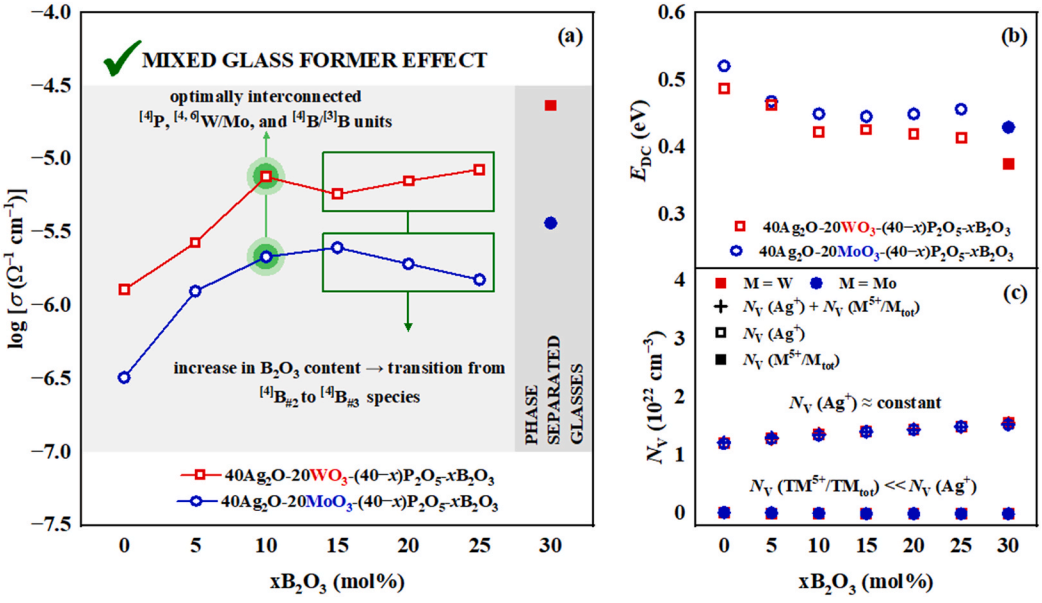

Fig. 13. Comparison of (A) DC conductivity, σ_{DC}, at 30 °C, (B) activation energy for DC conductivity, E_{DC}, and (C) number density, N_V, of Ag^+ ions as a function of B_2O_3 content for glasses from series $40Ag_2O$-$20WO_3$-$(40-x)P_2O_5$-xB_2O_3 and $40Ag_2O$-$20MoO_3$-$(40-x)P_2O_5$-xB_2O_3. The lines connecting data points in (A) are a guide for the eye.

At low B_2O_3 contents, borate species are incorporated predominantly into the phosphate-rich network rather than forming an independent borate subnetwork. This is reflected in the rapid increase in the number of P–O–B linkages and in the growing population of tetrahedral $^{[4]}B_{\#2}$ environments. The latter represent borate units connected through two bridging oxygen atoms and can contribute to both B–O–P and B–O–B bonding motifs. Their formation therefore promotes integration of the two glass-forming components and converts the parent phosphate network into a chemically mixed borophosphate framework.

The degree of structural mixing reaches its maximum in the intermediate-composition range, where both P–O–B connectivity and the $^{[4]}B_{\#2}$ population are highest. This region also corresponds to maxima in T_g and OPD, indicating that the formation of heteroatomic P–O–B linkages increases network cohesion and permits more efficient packing of the constituent structural units. The simultaneous increase in T_g and OPD is therefore consistent with a more strongly connected and compact glass network. Importantly, however, the enhanced ionic conductivity in this range cannot be rationalized by a simple free-volume argument, because structural densification would not inherently be expected to facilitate translational motion of Ag^+ ions. Although the maxima in T_g and oxygen packing density suggest a more compact and strongly interconnected glass network at intermediate B_2O_3 contents, these parameters cannot be directly related to the free volume accessible for Ag^+ migration. The enhanced ionic conductivity is accompanied by a reduction in the activation energy for DC transport, indicating more favourable conditions for ionic migration despite the increased structural packing density. This behaviour is consistent with changes in the local energy landscape experienced by Ag^+ ions as the phosphate and borate networks reorganize. However, the present data do not allow the individual contributions of free volume, Ag^+ site distribution, and migration-pathway connectivity to be quantitatively separated.

Instead, the nonlinear conductivity enhancement associated with the mixed glass-former effect appears to arise from a reorganization of the local potential-energy landscape experienced by the mobile Ag^+ ions. Formation of P–O–B linkages changes the distribution of non-bridging oxygen atoms, the local charge compensation requirements, and the chemical identity of the oxygen coordination environments surrounding Ag^+. The resulting structural disorder may generate a broader distribution of Ag^+ sites and lower the energetic mismatch between neighbouring coordination environments. In this interpretation, the mixed network enhances conductivity not by creating a more open structure, but by increasing the number of energetically accessible configurations for Ag^+ migration. The coincidence of the conductivity enhancement with maxima in P–O–B connectivity and $^{[4]}B_{\#2}$ population therefore suggests that mixed-network formation contributes substantially to the positive MGFE in the homogeneous glasses. However, because phosphate depolymerisation, borate speciation, and the non-bridging oxygen distribution change simultaneously with B_2O_3 content, the present correlations do not allow the contribution of P–O–B connectivity to be separated unambiguously from these concurrent structural changes.

The concurrent increase in T_g and ionic conductivity should not be interpreted as a direct relationship between network rigidity and Ag^+ mobility. While T_g reflects the cooperative structural relaxation of the glass network, ionic conductivity well below T_g is governed primarily by the local energy barriers and connectivity of accessible migration sites. Consequently, a more strongly interconnected glass network, as suggested by the increase in T_g, does not necessarily hinder Ag^+ transport. The observed maxima in both properties may instead reflect different consequences of the same underlying structural reorganization associated with the mixed phosphate–borate network.

The correlation is nevertheless not strictly proportional across the entire compositional range. Beyond the intermediate-B_2O_3 region, the number of P–O–B linkages and the $^{[4]}B_{\#2}$ population decrease, whereas trigonal borate species become increasingly dominant. The higher propensity of these $^{[3]}B$ units to form B–O–B linkages promotes development of a more internally connected borate-rich subnetwork and reduces the degree of atomic-scale mixing with the phosphate component. This structural reorganization is accompanied by fragmentation of the phosphate network and, at the highest B_2O_3 content, by the appearance of chemically distinct amorphous regions observed by electron microscopy. Thus, the high-B_2O_3 compositions no longer represent a continuation of the optimally mixed-network regime, but a transition toward mesoscale chemical heterogeneity.

The conductivity behaviour of the phase-separated compositions ($x = 30$) is particularly significant. Despite the decrease in the average P–O–B connectivity, these glasses retain, and in the WO_3-containing series further increase, their ionic conductivity. However, unlike the homogeneous compositions, the phase-separated glasses represent a distinct structural regime in which ionic transport may be strongly influenced by chemical partitioning and microstructure rather than solely by the connectivity of the mixed glass network.

SEM observations reveal droplets embedded in a continuous background phase, while EDX analysis of the WO_3-containing composition (Table S1) indicates that the background phase is enriched in W and P relative to the B-rich droplets and exhibits a higher Ag content relative to the network-forming cations. One possible explanation is therefore that long-range Ag^+ transport preferentially proceeds through this continuous phase, where the local concentration of mobile charge carriers and their coordination environments may differ from those

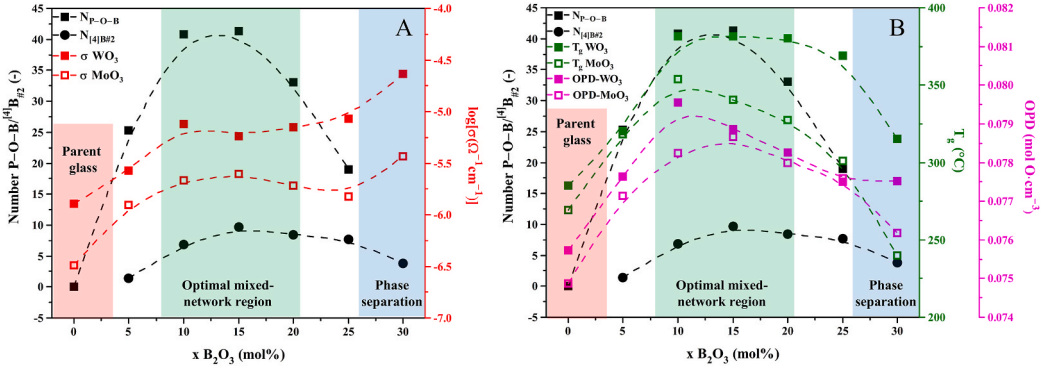

Fig. 14. Compositional evolution of structural, thermal, and transport properties in the $40Ag_2O$-$20MO_3$-$(40-x)P_2O_5$-xB_2O_3 glasses (M = W, Mo). (A) Number of P–O–B linkages (N_{P-O-B}), population of $^{[4]}B_{\#2}$ units ($N^{[4]}B_{\#2}$), and DC ionic conductivity (σ_{DC}) of the WO_3- and MoO_3-containing glass series. (B) Number of P–O–B linkages, population of $^{[4]}B_{\#2}$ units, glass transition temperature (T_g), and oxygen packing density (OPD) for both glass series. The shaded regions indicate the parent phosphate glass, the optimal mixed-network region associated with the positive nonlinear conductivity enhancement associated with the mixed glass-former effect, and the phase-separated region at high B_2O_3 contents. Dashed lines are guides to the eye. The estimated uncertainties of the NMR-derived $^{[4]}B_{\#2}$ populations and calculated P–O–B connectivities are ±2 percentage point and ±5, respectively.

expected from the nominal glass composition. Alternatively, the interfaces between chemically distinct amorphous domains may provide structurally disordered environments favourable for Ag^+ migration.

Although these observations support the possibility of different transport mechanisms in the phase-separated glasses, the present data do not establish the spatial distribution of ionic conductivity or the preferential migration pathways. Therefore, transport through the continuous Ag-enriched phase and transport along the interfaces remain plausible hypotheses rather than experimentally demonstrated mechanisms.

These results reveal two distinct composition-dependent strategies for enhancing ionic transport. The first is atomic-scale mixing of the phosphate and borate networks, characterized by maximized P–O–B connectivity and tetrahedral borate populations. The second, more tentative one, is the development of amorphous chemical heterogeneity at high B_2O_3 contents. The former offers a plausible, structurally well-supported explanation for the positive MGFE in homogeneous glasses, whereas the latter points to phase separation as an additional, potentially exploitable design parameter. Optimizing silver-conducting borophosphate glasses therefore requires control not only of the average network polymerisation, but also of heteroatomic connectivity and the length scale of chemical heterogeneity.

5. Conclusion

Silver borophosphate glasses belonging to the $40Ag_2O$-$20WO_3$-$(40-x)P_2O_5$-xB_2O_3 and $40Ag_2O$-$20MoO_3$-$(40-x)P_2O_5$-xB_2O_3 systems were investigated to establish composition–structure–property relationships governing ionic transport in mixed glass-former oxide electrolytes. The combined Raman, advanced multinuclear 1D/2D MAS NMR, EPR, and impedance spectroscopy results demonstrate that gradual substitution of P_2O_5 by B_2O_3 induces systematic reorganization of the glass network while preserving predominantly ionic Ag^+ conduction.

The structural evolution is controlled by the progressive transformation of the phosphate network, changes in borate speciation, and the extent of mixing between the phosphate and borate subnetworks. At intermediate B_2O_3 contents, the maximum concentration of P–O–B linkages and tetrahedral $^{[4]}B_{\#2}$ units coincides with maxima in glass transition temperature and oxygen packing density, along with a pronounced enhancement of ionic conductivity. These correlations indicate that mixed-network formation, rather than composition alone, plays a central role in the nonlinear property enhancement associated with the mixed glass-former effect in homogeneous silver borophosphate glasses. In contrast, higher B_2O_3 contents promote increasing B–O–B connectivity, development of borate-rich domains, and eventual amorphous phase separation.

Despite this structural transition, the phase-separated glasses retain high ionic conductivity, with the WO_3-containing composition exhibiting the highest conductivity within the investigated series. This observation suggests that the transport enhancement associated with phase separation may be governed by a mechanism different from that responsible for the nonlinear conductivity enhancement glass-former effect in homogeneous glasses. Although the nature of this mechanism remains to be established, the present results suggest that controlled amorphous chemical heterogeneity may provide an additional route for improving ionic transport in oxide glass electrolytes.

CRediT authorship contribution statement

Tomáš Hostinský: Writing – review & editing, Writing – original draft, Visualization, Methodology, Investigation, Formal analysis, Data curation, Conceptualization. **Petr Mošner:** Writing – review & editing, Validation, Supervision, Resources, Project administration, Methodology, Funding acquisition, Conceptualization. **Ladislav Koudelka:** Writing – review & editing, Writing – original draft, Validation, Supervision, Methodology, Investigation, Conceptualization. **Helena Drobná:** Methodology, Investigation, Formal analysis, Data curation. **Ludvík Beneš:** Visualization, Methodology, Investigation, Formal analysis. **Stanislav Slang:** Writing – review & editing, Visualization, Methodology, Investigation, Formal analysis, Data curation. **Adéla Jiříčková:** Investigation, Methodology, Visualization. **Lionel Montagne:** Writing – review & editing, Validation, Supervision, Methodology, Investigation, Conceptualization. **Andrew Rankin:** Writing – review & editing, Supervision, Methodology, Investigation, Data curation. **Gregory Tricot:** Writing – review & editing, Supervision, Methodology, Investigation, Data curation. **Hervé Vezin:** Visualization, Methodology, Investigation, Formal analysis, Data curation. **Maksym Buryi:** Writing – original draft, Visualization, Methodology, Investigation, Formal analysis, Data curation. **Sara Marijan:** Writing – review & editing, Writing – original draft, Visualization, Methodology, Investigation, Formal analysis, Data curation. **Luka Pavić:** Writing – review & editing, Writing – original draft, Visualization, Supervision, Methodology, Investigation, Formal analysis, Data curation, Conceptualization.

Declaration of generative AI in scientific writing

During the preparation of this work the author(s) used ChatGPT 5.6 Sol in order to improve the readability and language of the manuscript. After using this tool/service, the author(s) reviewed and edited the content as needed and take(s) full responsibility for the content of the published article.

Declaration of competing interest

The authors declare that they have no known competing financial interests or personal relationships that could have appeared to influence the work reported in this paper.

Acknowledgements

Authors would like to thank to project No. LM2023037 and Center of Materials and Nanotechnologies (CEMNAT) for the possibility of SEM imaging. The Chevreul Institute (CNRS UAR 2638), Ministère de l'Enseignement Supérieur, de la Recherche et de l'Innovation, Hauts-de-France Region, Métropole Européenne de Lille, and FEDER (European Union) are also acknowledged for supporting and partially funding this work, including *via* support for CPER projects. The French research facility Infranalytics (FR-2054) is acknowledged for the access to a high magnetic field. S.M. and L.P. would like to acknowledge support provided in part by the Croatian Science Foundation under Project No. IP-2025-02-7124 and by the internal Ruđer Bošković Institute (RBI) funding schemes ZI-2023/2023a (Program ZI5-25 and ZI5-26) implemented through the National Recovery and Resilience Plan 2021–2026 (NPOO) and funded by the European Union – NextGenerationEU.

Appendix A. Supplementary data

Supplementary data to this article can be found online at https://doi.org/10.1016/j.mtchem.2026.104187.

Data availability

Data will be made available on request.

References

[1] S.R. Keshri, S. Ganisetti, R. Kumar, A. Gaddam, K. Illath, T.G. Ajithkumar, S. Balaji, K. Annapurna, N. Nasani, N.M.A. Krishnan, A.R. Allu, Ionic conductivity of $Na_3Al_2P_3O_{12}$ glass electrolytes—role of charge compensators, Inorg. Chem. 60 (17) (2021) 12893–12905, https://doi.org/10.1021/acs.inorgchem.1c01280.

[2] S. Renka, L. Pavić, G. Tricot, P. Mošner, L. Koudelka, A. Moguš-Milanković, A. A. Šantić, Significant enhancement of sodium ion conductivity in phosphate glasses

by addition of WO_3 and MoO_3: the effect of mixed conventional–conditional glass-forming oxides, Phys. Chem. Chem. Phys. 23 (16) (2021) 9761–9772, https://doi.org/10.1039/D1CP00498K.
[3] M. Karlsson, M. Schuch, R. Christensen, P. Maass, S.W. Martin, S. Imberti, A. Matic, Structural origin of the mixed glass former effect in sodium borophosphate glasses investigated with neutron diffraction and reverse Monte carlo modeling, J. Phys. Chem. C 119 (49) (2015) 27275–27284, https://doi.org/10.1021/acs.jpcc.5b09176.
[4] R. Christensen, G. Olson, S.W. Martin, Ionic conductivity of mixed glass former $0.35Na_2O+0.65[\ xB_2O_3+(1–x)\ P_2O_5]$ glasses, J. Phys. Chem. B 117 (51) (2013) 16577–16586, https://doi.org/10.1021/jp409497z.
[5] M. Storek, R. Böhmer, S.W. Martin, D. Larink, H. Eckert, NMR and conductivity studies of the mixed glass former effect in lithium borophosphate glasses, J. Chem. Phys. 137 (12) (2012) 124507, https://doi.org/10.1063/1.4754664.
[6] M. Storek, M. Adjei-Acheamfour, R. Christensen, S.W. Martin, R. Böhmer, Positive and negative mixed glass former effects in sodium borosilicate and borophosphate glasses studied by ^{23}Na NMR, J. Phys. Chem. B 120 (19) (2016) 4482–4495, https://doi.org/10.1021/acs.jpcb.6b00482.
[7] A. Magistris, G. Chiodelli, M. Duclot, Silver borophosphate glasses : ion transport, thermal stability and electrochemical behaviour, Solid State Ion 9–10 (1983) 611–615, https://doi.org/10.1016/0167-2738(83)90303-X.
[8] G. Chiodelli, A. Magistris, M. Villa, Ionic conductivity and glass transition of borophosphate glasses, Solid State Ion 18–19 (1986) 356–361, https://doi.org/10.1016/0167-2738(86)90140-2.
[9] S. Kabi, A. Ghosh, Mixed glass former effect in AgI doped silver borophosphate glasses, Solid State Ion 262 (2014) 778–781, https://doi.org/10.1016/j.ssi.2013.09.028.
[10] V.A. Adhwaryu, D.K. Kanchan, Ag^+ ion conduction in AgI- Ag_2O-B_2O_3-P_2O_5 glass electrolyte, Mater. Sci. Eng. B 263 (2021) 114857, https://doi.org/10.1016/j.mseb.2020.114857.
[11] S. Elbers, W. Strojek, L. Koudelka, H. Eckert, Site Connectivities in Silver Borophosphate Glasses: New Results from $^{11}B\{^{31}P\}$ and $^{31}P\{^{11}B\}$ Rotational Echo Double Resonance NMR Spectroscopy, Solid State Nucl. Magn. Reson. 27 (1) (2005) 65–76, https://doi.org/10.1016/j.ssnmr.2004.08.007.
[12] N. Machida, A. Ueda, H. Tanaka, T. Shigematsu, N. Nakanishi, M. Takahashi, T. Minami, The structure of AgI-Ag_2MoO_4-$Ag_2PO_{3.5}$ glasses studied by ^{31}P Magic Angle Spinning (MAS) NMR and Their Silvtr IonsConduciingcProperties, J. Non-Cryst. Solids 192–193 (1995) 326–329, https://doi.org/10.1016/0022-3093(95)00370-3.
[13] N. Machida, Mixed anion effect of silver ion conducting glasses in the systems AgI-Ag_2MoO_4-Ag_3PO_4 and AgI-Ag_2MoO_4-$Ag_2PO_{3.5}$ and structural study by ^{31}P MAS-NMR, Solid State Ion 79 (1995) 273–278, https://doi.org/10.1016/0167-2738(95)00073-F.
[14] L. Koudelka, I. Rösslerová, J. Holubová, P. Mošner, L. Montagne, B. Revel, Structural study of PbO–MoO_3–P_2O_5 glasses by raman and NMR spectroscopy, J. Non-Cryst. Solids 357 (15) (2011) 2816–2821, https://doi.org/10.1016/j.jnoncrysol.2011.03.006.
[15] L. Koudelka, I. Rösslerová, Z. Černošek, P. Mošner, Structure and properties of lead tungstate phosphate glasses, Phys. Chem. Glas. - Eur. J. Glass Sci. Technol. Part B 53 (3) (2012) 86–92.
[16] L. Koudelka, P. Kalenda, J. Holubová, P. Mošner, L. Montagne, B. Revel, Structural study of BaO-MoO_3-P_2O_5 glasses by raman and NMR spectroscopy, J. Non-Cryst. Solids 476 (2017) 114–121, https://doi.org/10.1016/j.jnoncrysol.2017.09.040.
[17] P. Mošner, O. Kupetska, L. Koudelka, Sodium phosphate glasses modified by MoO_3 and WO_3, Phys. Chem. Glas. Eur. J. Glass Sci. Technol. Part B 59 (5) (2018) 213–220, https://doi.org/10.13036/17533562.59.5.020.
[18] L. Koudelka, T. Hostinský, P. Mošner, L. Montagne, B. Revel, M. Buryi, L. Pavić, Structure and properties of silver phosphate glasses with tungsten trioxide, J. Non-Cryst. Solids 682 (2026) 124080, https://doi.org/10.1016/j.jnoncrysol.2026.124080.
[19] D. Massiot, F. Fayon, M. Capron, I. King, S. Le Calvé, B. Alonso, J. Durand, B. Bujoli, Z. Gan, G. Hoatson, Modelling one- and two-dimensional solid-state NMR spectra, Magn. Reson. Chem. 40 (1) (2002) 70–76, https://doi.org/10.1002/mrc.984.
[20] A. Lesage, M. Bardet, L. Emsley, Through-bond carbon−carbon connectivities in disordered solids by NMR, J. Am. Chem. Soc. 121 (47) (1999) 10987–10993, https://doi.org/10.1021/ja992272b.
[21] S. Stoll, A. EasySpin Schweiger, A comprehensive software package for spectral simulation and analysis in EPR, J. Magn. Reson. 178 (1) (2006) 42–55, https://doi.org/10.1016/j.jmr.2005.08.013.
[22] L. Koudelka, P. Kalenda, P. Mošner, Z. Černošek, L. Montagne, B. Revel, Structural investigation of BaO-B_2O_3-P_2O_5 glasses by NMR and Raman spectroscopy, J. Mol. Struct. 1119 (2016) 212–219, https://doi.org/10.1016/j.molstruc.2016.04.066.
[23] P. Mošner, T. Hostinský, L. Koudelka, M. Razum, L. Pavić, L. Montagne, B. Revel, Structure-property correlation in sodium borophosphate glasses modified with niobium oxide, Coatings 12 (11) (2022) 1626, https://doi.org/10.3390/coatings12111626.
[24] R.K. Brow, D.R. Tallant, Structural design of sealing glasses, J. Non-Cryst. Solids 222 (1997) 396–406, https://doi.org/10.1016/S0022-3093(97)90142-3.
[25] T. Hostinský, L. Koudelka, P. Mošner, G. Tricot, H. Drobná, M. Razum, A. Šantić, The influence of B_2O_3 on structure and ionic conductivity of lithium phosphate-niobate glasses, J. Non-Cryst. Solids 646 (2024) 123258, https://doi.org/10.1016/j.jnoncrysol.2024.123258.
[26] B. Doumert, F. Lecomte, G. Tricot, Advanced solid state 1D/2D NMR investigation of the B_2O_3-$Zn(PO_3)_2$ glasses, J. Non-Cryst. Solids 548 (2020) 120325, https://doi.org/10.1016/j.jnoncrysol.2020.120325.
[27] D.R. Lide (Ed.), CRC Handbook of Chemistry and Physics: a Ready-Reference Book of Chemical and Physical Data, 88, CRC Press, Boca Raton, Fla, 2008.
[28] R.K. Brow, Review: the structure of simple phosphate glasses, J. Non-Cryst. Solids 263–264 (2000) 1–28, https://doi.org/10.1016/S0022-3093(99)00620-1.
[29] J.J. Hudgens, R.K. Brow, D.R. Tallant, S.W. Martin, Raman spectroscopy study of the structure of lithium and sodium ultraphosphate glasses, J. Non-Cryst. Solids 223 (1) (1998) 21–31, https://doi.org/10.1016/S0022-3093(97)00347-5.
[30] I.J. Hidi, G. Melinte, R. Stefan, M. Bindea, L. Baia, The study of the structure and bioactivity of the $B_2O_3 \bullet Na_2O \bullet P_2O_5$ system, J. Raman Spectrosc. 44 (8) (2013) 1187–1194, https://doi.org/10.1002/jrs.4330.
[31] J. Ren, H. Eckert, Quantification of short and medium range order in mixed network former glasses of the system GeO_2–$NaPO_3$: a combined NMR and X-Ray photoelectron spectroscopy study, J. Phys. Chem. C 116 (23) (2012) 12747–12763, https://doi.org/10.1021/jp301383x.
[32] P.T. Freudenberger, R.L. Blatt, R.E. Youngman, R.K. Brow, Network structures and the properties of Na-Ca-Sr-Borophosphate glasses, J. Non-Cryst. Solids 600 (2023) 121966, https://doi.org/10.1016/j.jnoncrysol.2022.121966.
[33] S. Renka, R.D. Banhatti, G. Tricot, P. Kalenda, L. Pavić, P. Mošner, L. Koudelka, A. Šantić, Glass structure as a driver of polaronic conductivity in phosphate glasses containing MoO_3 and WO_3, J. Mater. Chem. C 11 (28) (2023) 9628–9639, https://doi.org/10.1039/D3TC00954H.
[34] A. Šantić, J. Nikolić, S. Renka, L. Pavić, P. Mošner, L. Koudelka, G. Tricot, A. Moguš-Milanković, A versatile role of WO_3 and MoO_3 in electrical transport in phosphate glasses, Solid State Ion 375 (2022) 115849, https://doi.org/10.1016/j.ssi.2021.115849.
[35] C. C. de Araujo, W. Strojek, L. Zhang, H. Eckert, G. Poirier, S.J.L. Ribeiro, Y. Messaddeq, Structural studies of $NaPO_3$–WO_3 glasses by solid state NMR and Raman spectroscopy, J. Mater. Chem. 16 (32) (2006) 3277–3284, https://doi.org/10.1039/B605971F.
[36] S. Renka, G. Tricot, T. Hostinský, P. Mošner, L. Koudelka, A. Ibrahim, S. Kubuki, Z. Siketić, A. Šantić, Tailoring a glass network structure through addition of transition metal oxides to enhance ionic conductivity in phosphate glasses, Inorg. Chem. 64 (23) (2025) 11412–11425, https://doi.org/10.1021/acs.inorgchem.5c00313.
[37] S.H. Santagneli, C.C. de Araujo, W. Strojek, H. Eckert, G. Poirier, S.J.L. Ribeiro, Y. Messaddeq, Structural studies of $NaPO_3$−MoO_3 glasses by solid-state nuclear magnetic resonance and Raman spectroscopy, J. Phys. Chem. B 111 (34) (2007) 10109–10117, https://doi.org/10.1021/jp072883n.
[38] Z. Zhang, J. Ren, L. Hu, Fast ionic conducting glasses in the system 20LiCl–40Li_2O–(80–x)$PO_{5/2}$–xMoO_3: the structural dependence of ion conductivity studied by solid-state nuclear magnetic resonance spectroscopy, J. Phys. Chem. C 124 (12) (2020) 6528–6535, https://doi.org/10.1021/acs.jpcc.0c00171.
[39] K. Bodiang, L. Delevoye, R. Podor, F.O. Méar, Role of molybdenum on the structure and properties of A_2O-P_2O_5−MoO_3 (A = Na, Ag, Rb, cs) glasses, J. Non-Cryst. Solids 606 (2023) 122193, https://doi.org/10.1016/j.jnoncrysol.2023.122193.
[40] P. Mustarelli, The nmr information on phosphate glasses: a review, Phosphorus Res. Bull. 10 (1999) 25–36, https://doi.org/10.3363/prb1992.10.0_25.
[41] L. Koudelka, P. Mošner, J. Jirák, M. Zeyer-Düsterer, C. Jäger, Medium range order in lead borophosphate glasses, Phys. Chem. Glas. Eur. J. Glass Sci. Technol. Part B 47 (4) (2006) 471–475.
[42] B.K. Money, K. Hariharan, Glass formation and electrical conductivity studies of melt quenched and mechanically milled 50Li_2O:(50−x) P_2O_5:xB_2O_3, Solid State Ion 179 (27–32) (2008) 1273–1277, https://doi.org/10.1016/j.ssi.2007.12.068.
[43] F. Muñoz, L. Montagne, L. Pascual, A. Durán, Composition and structure dependence of the properties of lithium borophosphate glasses showing Boron Anomaly, J. Non-Cryst. Solids 355 (52) (2009) 2571–2577, https://doi.org/10.1016/j.jnoncrysol.2009.09.013.
[44] B. Raguenet, G. Tricot, G. Silly, M. Ribes, A. Pradel, Revisiting the 'Mixed Glass Former Effect' in ultra-fast quenched borophosphate glasses by advanced 1D/2D solid state NMR, J. Mater. Chem. 21 (44) (2011) 17693–17704, https://doi.org/10.1039/C1JM12350E.
[45] B. Raguenet, G. Tricot, G. Silly, M. Ribes, A. Pradel, The mixed glass former effect in twin-roller quenched lithium borophosphate glasses, Solid State Ion 208 (2012) 25–30, https://doi.org/10.1016/j.ssi.2011.11.034.
[46] L. Muñoz-Senovilla, G. Tricot, F. Muñoz, Kinetic fragility and structure of lithium borophosphate glasses analysed by 1D/2D NMR, Phys. Chem. Chem. Phys. 19 (34) (2017) 22777–22784, https://doi.org/10.1039/C7CP04171C.
[47] L. Koudelka, J. Pospíšil, P. Mošner, L. Montagne, L. Delevoye, Structure and properties of potassium Niobato-Borophosphate glasses, J. Non-Cryst. Solids 354 (2) (2008) 129–133, https://doi.org/10.1016/j.jnoncrysol.2007.07.030.
[48] G. Tricot, K. Ben Tayeb, L. Koudelka, P. Mosner, H. Vezin, Insertion of MoO3 in borophosphate glasses investigated by magnetic resonance spectroscopies, J. Phys. Chem. C 120 (17) (2016) 9443–9452, https://doi.org/10.1021/acs.jpcc.6b02502.
[49] M. Villa, K.R. Carduner, G. Chiodelli, A ^{31}P-NMR Study of Borophosphbte Glasses, Jg Solid State Chem. 69 (1) (1987) 19–23, https://doi.org/10.1016/0022-4596(87)90004-1.
[50] Y. Watanabe, K. Hayashi, G. Tricot, B. Doumert, A. Saitoh, Structural insights into properties of SnO–P_2O_5–B_2O_3 glasses: P_2O_5/B_2O_3 substitution effect, Mater. Chem. Phys. 323 (2024) 129641, https://doi.org/10.1016/j.matchemphys.2024.129641.
[51] M. Zeyer-Düsterer, L. Montagne, G. Palavit, C. Jäger, Combined ^{17}O NMR and ^{11}B–^{31}P Double Resonance NMRdStudier of Sodium BosophosphatesGlasseb, Solid StategNucl. Magn. Reson. 27 (1–2) (2005) 50–64, https://doi.org/10.1016/j.ssnmr.2004.06.009.
[52] A. Saitoh, G. Tricot, P. Rajbhandari, S. Anan, H. Takebe, Effect of B_2O_3/P_2O_5 substitution on the properties and structure of tin boro-phosphate glasses, Mater.

Chem. Phys. 149–150 (2015) 648–656, https://doi.org/10.1016/j.matchemphys.2014.11.021.
[53] A. Abragam, B. Bleaney, Electron Paramagnetic Resonance of Transition Ions, Repr.; the International Series of Monographs on Physics, Oxford Univ. Press, Oxford, 2013.
[54] C.P. Poole, H.A. Farach, Handbook of Electron Spin Resonance. 2, American Inst. of Physics, New York, 1999.
[55] V.V. Laguta, M. Buryi, M. Nikl, J. Rosa, S. Zazubovich, Hole capture in $PbWO_4$:Mo, La(Y) scintillator crystals, Phys. Rev. B 83 (9) (2011) 094123, https://doi.org/10.1103/PhysRevB.83.094123.
[56] M. Buryi, V. Laguta, M. Fasoli, F. Moretti, K. Jurek, M. Trubitsyn, M. Volnianskii, S. Nagorny, V. Shlegel, A. Vedda, M. Nikl, Charge trapping processes and energy transfer studied in lead molybdate by EPR and TSL, J. Lumin. 205 (2019) 457–466, https://doi.org/10.1016/j.jlumin.2018.09.052.
[57] G.H. Fuller, Nuclear spins and moments, J. Phys. Chem. Ref. Data 5 (4) (1976) 835–1092, https://doi.org/10.1063/1.555544.
[58] S.A. Al'tshuler, B.M. Kozyrev, C.P. Poole, Electron Paramagnetic Resonance, Academic Press, New York and London, 1964.
[59] V. Jarý, L. Havlák, J. Bárta, M. Buryi, E. Mihóková, M. Rejman, V. Laguta, M. Nikl, Optical, structural and paramagnetic properties of Eu-Doped ternary sulfides $ALnS_2$ (A = Na, K, Rb; Ln = La, Gd, Lu, Y), Materials 8 (10) (2015) 6978–6998, https://doi.org/10.3390/ma8105348.
[60] J.E. Wertz, J.R. Bolton, Electron Spin Resonance: Elementary Theory and Practical Applications, Chapman and Hall, New York, New York ; London, [England], 1986.
[61] D. Zielniok, C. Cramer, H. Eckert, Structure/property correlations in ion-conducting mixed-network former glasses: Solid-state NMR studies of the system $Na_2O–B_2O_3–P_2O_5$, Chem. Mater. 19 (13) (2007) 3162–3170, https://doi.org/10.1021/cm0628092.
[62] A. Magistris, G. Chiodelli, M. Villa, Lithium borophosphate vitreous electrolytes, J. Power Sources 14 (1–3) (1985) 87–91, https://doi.org/10.1016/0378-7753(85)88016-2.
[63] K. Sklepić, R.D. Banhatti, G. Tricot, P. Mošner, L. Koudelka, A. Moguš-Milanković, Insights from local network structures and localized diffusion on the ease of lithium ion transport in two mixed glass-former systems, J. Phys. Chem. C 121 (33) (2017) 17641–17657, https://doi.org/10.1021/acs.jpcc.7b05108.
[64] K. Sklepić, G. Tricot, P. Mošner, L. Koudelka, A. Moguš-Milanković, Sodium ion conductivity in mixed former $Na_2O–P_2O_5–GeO_2$ and $Na_2O–B_2O_3–P_2O_5–GeO_2$ glasses, J. Phys. Chem. C 125 (19) (2021) 10593–10604, https://doi.org/10.1021/acs.jpcc.1c00072.
[65] I.G. Austin, N.F. Mott, Polarons in crystalline and non-crystalline materials, Adv. Phys. 18 (71) (1969) 41–102, https://doi.org/10.1080/00018736900101267.
[66] L. Murawski, C.H. Chung, J.D. Mackenzie, Electrical properties of semiconducting oxide glasses, J. Non-Cryst. Solids 32 (1–3) (1979) 91–104, https://doi.org/10.1016/0022-3093(79)90066-8.
[67] J. Nikolić, A. Šantić, L. Pavić, D. Pajić, P. Mošner, L. Koudelka, A. Moguš-Milanković, Mixed ion-polaron glasses as new cathode materials, Croat. Chem. Acta 90 (4) (2017), https://doi.org/10.5562/cca3330.
[68] L. Pavić, A. Šantić, J. Nikolić, P. Mošner, L. Koudelka, D. Pajić, A. Moguš-Milanković, Nature of mixed electrical transport in $Ag_2O–ZnO–P_2O_5$ glasses containing WO_3 and MoO_3, Electrochim. Acta 276 (2018) 434–445, https://doi.org/10.1016/j.electacta.2018.04.029.
[69] A. Šantić, J. Nikolić, L. Pavić, R.D. Banhatti, P. Mošner, L. Koudelka, A. Moguš-Milanković, Scaling features of conductivity spectra reveal complexities in ionic, polaronic and mixed ionic-polaronic conduction in phosphate glasses, Acta Mater. 175 (2019) 46–54, https://doi.org/10.1016/j.actamat.2019.05.067.